Fast and controllable topological excitation transfers in hybrid magnon-photon systems

Jin-Xuan Han,[1] Jin-Lei Wu,[2,*] Zhong-Hui Yuan,[1] Yong-Jian Chen,[1] Yan Xia,[3] Yong-Yuan Jiang,[1] and Jie Song[1,4,5,6,†]

[1] *School of Physics, Harbin Institute of Technology, Harbin 150001, China*

[2] *School of Physics and Microelectronics, Zhengzhou University, Zhengzhou 450001, China*

[3] *Department of Physics, Fuzhou University, Fuzhou 350002, China*

[4] *Key Laboratory of Micro-Nano Optoelectronic Information System, Ministry of Industry and Information Technology, Harbin 150001, China*

[5] *Key Laboratory of Micro-Optics and Photonic Technology of Heilongjiang Province, Harbin Institute of Technology, Harbin 150001, China*

[6] *Collaborative Innovation Center of Extreme Optics, Shanxi University, Taiyuan, Shanxi 030006, People's Republic of China*

(Received 18 September 2022; revised 22 November 2023; accepted 9 January 2024; published 29 January 2024)

Hybridized magnonic-photonic systems are key components for future information-processing technologies such as storage, manipulation, or conversion of data in the quantum regime owing to its ability to achieve collective excitation of spin waves and excellent properties of low damping rate, high spin density, and highly tunable excitations. We propose to realize fast and controllable topological single- and multi-excitation quantum state transfers (QSTs) through a magnon-circuit-QED chain. Various time-dependent magnon-photon and photon-photon couplings are tailored via the Kerr nonlinearity of the magnons and superconducting quantum interference devices, which are implemented fast magnon-magnon excitation transfers by mapping the system to a Su-Schrieffer-Heeger model. We analytically derive the edge state of the system, qualitatively explain the mechanism of fast QST, and numerically show the robustness of QST against on-site potential defects, the fluctuation of couplings, and losses of the system. Furthermore, when larger on-site defects are added to different types of lattice sites in the two ends, alternative single-excitation controllable magnon-photon, photon-magnon, and photon-photon transfers are also accessible. Our work opens up prospects for realizing a fast and controllable quantum channel in magnon-circuit-QED system and for facilitating further applications of topological matter in robust quantum information processing in magnonics and photonics.

DOI: 10.1103/PhysRevApplied.21.014057

I. INTRODUCTION

Excitation transfer in classical and quantum networks is of great significance in numerous applications from coherent control of chemical reactions [1] and efficient excitation transfer in organic molecules [2] to quantum state transfer (QST) and large-scale quantum information processing [3–9]. For the latter application, quantum states need to be coherently and robustly transferred between distant nodes in a quantum network, which triggers great efforts on techniques to shape perfect QST in various physical platforms [3–5,10–20], such as photon pulse shaping of an atom-coupled optical cavity [10,11], transferring via spin chains and spin-wave engineering [3–5], frequency conversion via an optomechanical interface [12], quantum error correction [13,14], applying time-dependent control fields in quantum dot network [15], adiabatic and superadiabatic QST schemes [16–20]. However, a major challenge facing the field of QST arises from the delicate nature of a quantum system, their perturbation and decoherence process of the systems and environment.

In quantum information processing, fast readout of a long-lifetime qubit requires delicate isolation and shielding between the qubit and the circuit [21–23]. This remains a great challenge [24–28] because even a tiny amount of energy leakage would spoil the sensitive quantum state [21]. Superconducting integrated circuits [29] are special owing to the ease of scaling up to multiqubit networks and being integrated to other quantum modules. Recently,

*jlwu517@zzu.edu.cn
†jsong@hit.edu.cn

the hybrid system containing magnons has attracted a lot of attention [30–37]. Magnon, i.e., spin-wave quanta, are collective excitations of exchange-coupled spins in magnetic materials. Because the spin density of magnetic materials is higher than that of individual spins, large and tunable magnetic dipole coupling strengths can be obtained between magnons and microwave photons [35,38–41], which means that rapid operation and conversion can be achieved before decoherence. For the Kittel mode in the YIG sphere, the magnons are collective excitations of spins with zero wave number (i.e., in the long-wavelength limit) where all exchange-coupled spins in the sample precess uniformly [42]. The magnon has been considered as the quantum information carrier to realize functions for storage, transmission, and processing [43]. In the microwave region, the ferromagnetic spin ensemble in the YIG sphere is an easily tunable system with the benefits of flexible and wide-range adjustability of the magnon mode frequency (a few hundred megahertz to several tens of gigahertz), low dissipation at room temperature [26,44–47], and extendibility by constructing the magnon-based hybrid system [34,48–51]. The above distinct advantages of magnon-circuit-QED system allow for the photon in the microwave cavity acting as the fly qubit as well as the magnon in the YIG sphere regarding as the storage qubit, constituting a key step for future quantum communication networks.

Recently, topological QST methods have attracted great interest owing to the opportunity to harvest topological phenomena for guiding and transmitting quantum information reliably [52–60]. For instance, the Su-Schrieffer-Heeger (SSH) model, originally describing transport properties of the conductive polyacetylene [61], provides perhaps the most basic model supporting topological transfer of excitations protected by chiral symmetry [52,55,57–60]. Topological QST protocols in SSH chains rely on adiabatic techniques and operate on edge states, whose eigenenergies are distant from the bulk state. These procedures have shown a good resilience against uncorrelated disorder, but their speed is intrinsically limited by the adiabaticity requirement to avoid unwanted nonadiabatic transitions. So far, there are several kinds of techniques to realize fast topological QSTs to limit the impact of decoherence as the following. (i) Fast topological QSTs rely on shortcuts to adiabaticity techniques, where specifically engineered terms are introduced in the Hamiltonian that can induce counterprocesses able to suppress the excitations [62]. (ii) The adiabatic passage formed by interfacing two dimerized SSH chains with different topological order can realize fast topological pumping to further improve the efficiency of topological QSTs [63]. (iii) The existence of a zero-energy interface state in a splicing SSH chain can improve the transfer speed [64]. (iv) Optimization techniques on exponential time-driving coupling depend on the trade-off between speed and robustness under the adiabatic limit to realize fast topological QSTs [65]. However, these are either too slow for the intended application as well as subject to decoherence effects in quantum system or lacking a detailed introduction of fast topological QST mapping into a real physical platform as well as how to extend types of topological QST in hybrid systems, which remains unexplored.

In this work, we consider a magnon-circuit-QED hybrid system to realize fast and controllable QST via topological edge channels in case of not only single excitation but also multiple excitations of magnon-magnon transfer, where the model is an odd-sized SSH chain consisting of two YIG spheres in the ends and $2N-3$ superconducting resonators in the middle. In addition to hybridization between magnons and microwave photons, the nonlinear effect originating from the magnetocrystalline anisotropy in the YIG sphere [66] can realize tunable magnon-photon coupling and the superconducting quantum interference devices (SQUIDs) to realize the tunable photon-photon coupling, respectively, making the magnon-circuit-QED chain versatile to simulate models of topological matters and further to realize fast and controllable topological single-excitation QSTs. By mapping magnon-circuit-QED chain into a standard SSH model through quantization processes, we analytically derive that the hybrid system can be expressed as a two-band structure in momentum space, and its topologically nontrivial and trivial phases can be characterized by the Zak phases equal to 0 and π, respectively. Furthermore, according to the energy spectrum characteristics of the system, the time-dependent couplings between Kittel mode in the YIG sphere and microwave photon mode in the superconducting resonator are properly shaped as a linear function, a tangential function and a three-step function, respectively, so that fast topological magnon-magnon QSTs can be realized through the edge channel to different degrees. The numerical results show that the three-step protocol demonstrates the fastest topological magnon-magnon QST with transfer duration being shorter than one seventeenth of that of the commonly used trigonometric protocol. Furthermore, alternative diverse controllable transfers can be induced by the corresponding on-site potential defects on YIG spheres or/and superconducting resonators. To be specific, when larger on-site potential defects are added to the first and penultimate or the second and last lattice sites, the magnon-photon QST or the photon-magnon QST can be generated by the topological protected edge channel. In addition, the head and the tail on-site potential defects are taken into the magnon-QED-circuit chain in order to form the topological protected photon-photon QST. The present work may provide theoretical and experimental prospects for realizing fast and controllable topological quantum channel in the magnon-circuit-QED hybrid system and further applications in robust and controllable quantum information processing.

II. PHYSICAL MODEL AND ENGINEERING OF TOPOLOGICAL PUMPING

A. Hybrid system in the nanocircuit

The schematic of the SSH model is shown in Fig. 1(a), which can describe a one-dimensional magnon-circuit-QED hybrid system composed of two YIG spheres, which are in the head and the tail lattice cells and $2N-2$ superconducting resonators in the middle lattice cells of the chain. In this chain, the first (last) unit cell contains two sublattice sites, which are the YIG sphere A_1 (A_N) and the resonator B_1 (B_N). The remaining unit cells contain two different types of resonators A_n and B_n for $n \in [2, N-1]$. The intracell and intercell coupling strengths are J_1 and J_2, respectively. The SSH chain can be described by Hamiltonian

$$H_I = \sum_{n=1}^{N} \left(J_1 a_n^{\dagger} b_n + J_2 a_{n+1}^{\dagger} b_n\right) + \text{H.c.}, \tag{1}$$

where $a_{1,N}$, a_n ($n \neq 1, N$), and b_n are annihilation operators of the magnon mode in the YIG sphere $A_{1,N}$ and the photon mode in two different types of superconducting resonator A_n and B_n, respectively.

According to existing magnon-circuit-QED technologies [30–34,45,67], one can construct a chain to arrange two YIG spheres in the head and tail lattice cells and superconducting resonators in the middle lattice cells of the chain in one-dimensional space, whose equivalent circuit design of the magnon mode of the YIG sphere coupling to the photon mode in the superconducting resonator is shown in Fig. 1(b). In addition, the YIG sphere is directly pumped by a microwave field with the Rabi frequency Ω and the frequency ω_d. In experiment, a drive coil near the YIG sample goes out of the resonator through one port of the resonator connected to a microwave source [68]. The YIG sphere is mounted at the deep hole, which are etched on the Si substrate, matching the dimension of the YIG sphere. The magnons embodied by a collective motion of a large number of spins in a ferrimagnet can be provided by a YIG sphere. At the same time, an external

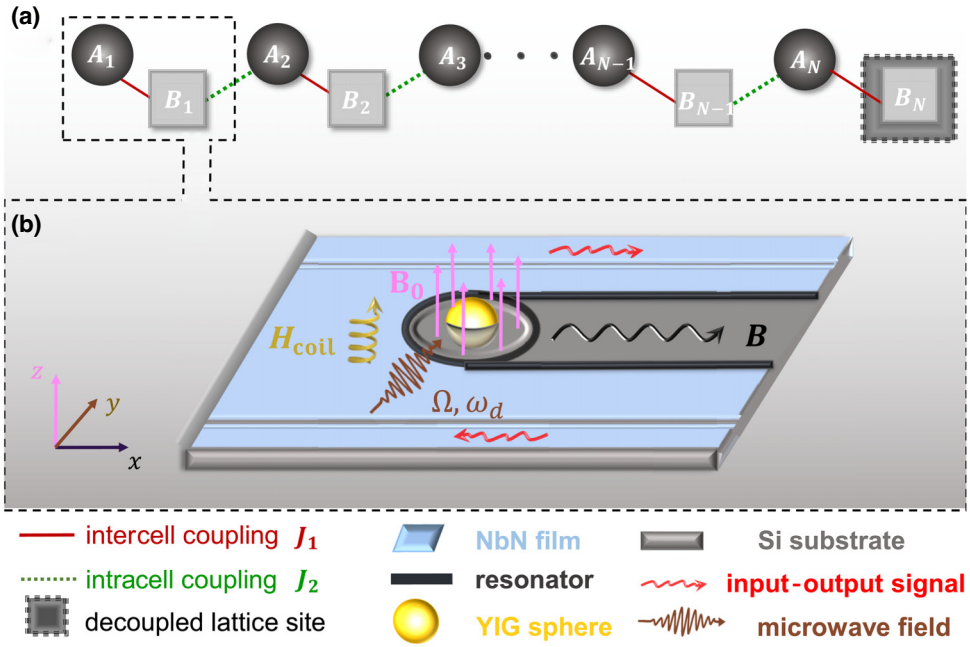

FIG. 1. (a) The diagrammatic sketch of a magnon-QED-circuit hybrid system with the size of $2N$ in the one-dimensional space. The chain belongs to an SSH model whose first (last) unit cell contains one YIG sphere A_1 (A_N) and one superconducting resonator B_1 (B_N) and the remaining unit cells contain two different types of resonators A_n and B_n, respectively, for $n \in [2, N-1]$. The intracell and intercell coupling strengths are J_1 and J_2, respectively. (b) Sketch of a YIG sphere coupled to a superconducting resonator. The hybrid superconducting circuit is defined by photolithography and reactive ion etching, which is fabricated from NbN film sputtered on a high-resistance Si substrate [34]. The probe microwave signal is received or sent from a network analyzer and amplified or attenuated by in the output or input signal line, which is placed in a dilution refrigerator (with a temperature $T \sim$ mK). A YIG sphere magnetized to saturation, where the Kittle mode of magnon is excited by an external magnetic field $\mathbf{B}_0$ along the z axis, is mounted at the center of the loop in the superconducting resonator. The magnetic field $\mathbf{B}$ of the superconducting resonator is along the x direction to excite the magnon mode in the YIG sphere. The magnon mode is driven by a microwave field with the Rabi frequency Ω and driving frequency ω_d along the y direction. The local NbTi superconducting coil adjacent to one YIG sphere for individual magnon frequency control. The superconducting resonator is realized by an LC circuit, consisting of a capacitor C connected in series with an inductor L.

magnetic field $\mathbf{B}_0$ magnetizes the YIG sphere to saturation and then induces the Kittel mode of magnons in the YIG sphere [69]. The superconducting resonator is composed of a spiral inductor L and a capacitor C in analogy with an LC harmonic oscillator. The Zeeman effect is achieved by placing a YIG sphere in the superconducting resonator so that it overlaps with the microwave magnetic field of the superconducting resonator. To allow for individual magnon frequency control, a local NbTi superconducting coil adjacent to one YIG sphere is integrated to generate the coil magnetic field $\mathbf{H}_{\text{coil}}$ onto the nearby YIG sphere without Ohmic heating in the cryogenic environment [34].

The hybrid system of the first and last unit cell in the chain shown in Fig. 1(b) consists of a YIG sphere and a superconducting resonator. We study the Kittel mode in the YIG sphere, which is strongly coupled to superconducting resonator. At the same time, the Kittel mode is driven by a microwave field. The Hamiltonian for the whole system reads

$$\begin{aligned} H_{\text{YIG}} &= -\int \mathbf{M}\cdot\mathbf{B}_0 d\tau - \frac{\mu_0}{2}\int \mathbf{M}\cdot(\mathbf{H}_{\text{d}}+\mathbf{H}_{\text{an}})d\tau, \\ H_{LC} &= \frac{Q^2}{2C}+\frac{\Phi^2}{2L}, \\ H_{\text{int}} &= -\mu_0\int \mathbf{M}\cdot\mathbf{B}d\tau. \end{aligned} \tag{2}$$

For H_{YIG}, $\mathbf{B}_0 = B_0\mathbf{e}_z$ is the applied static magnetic field, μ_0 is the vacuum permeability, $\mathbf{M} = \hbar\gamma_m\mathbf{S}/V_m$ is the magnetization of the YIG sphere, with γ_m, V_m, and $\mathbf{S} \equiv (S_x, S_y, S_z)$ denoting the gyromagnetic ratio, the volume of the YIG sphere and the collective spin operator [70, 71], $\mathbf{H}_{\text{d}} = -B_d\cos(\omega_d t)\mathbf{e}_y$ is the driving microwave field with driving frequency ω_d and amplitude B_d to pump the YIG sphere (i.e., the macrospin), $\mathbf{H}_{\text{an}} = -(2K_{\text{an}}M_z/M^2)\mathbf{e}_z$ is the anisotropic field due to the magnetocrystalline anisotropy and has only a z component owing to the 100 crystallographic axis being aligned along the applied static magnetic field [66], K_{an} is the dominant first-order anisotropy constant, and M is the saturation magnetization [68]. For H_{LC}, Φ is the flux through the inductor L and Q the charge on the capacitor C. For H_{int}, $\mathbf{B}$ is the corresponding magnetic field are along the x axis inside the LC resonator. Based on the standard quantization process of an LC circuit [72], a pair of conjugate variables Q and Φ are satisfied with the canonical commutation relation $[Q, \Phi] = i\hbar$, which can be defined by

$$\begin{aligned} Q &= \sqrt{\frac{\omega_b C}{2}}(b^\dagger + b), \\ \Phi &= i\sqrt{\frac{\omega_b L}{2}}(b^\dagger - b), \end{aligned} \tag{3}$$

where $\omega_b = 1/\sqrt{LC}$ is the oscillator frequency and can be engineered in a large range of possible values by adjusting the parameters L and C.

The Holstein-Primakoff transform yields [73]

$$\begin{aligned} S_z &= S - a^\dagger a, \\ S^+ &= a\sqrt{2S - a^\dagger a}, \\ S^- &= a^\dagger\sqrt{2S - a^\dagger a}, \end{aligned} \tag{4}$$

where a is the bosonic (magnon) annihilation operator and $S_\pm \equiv S_l^x \pm iS_l^y$. For a micrometer-scale YIG sphere with spin density $\rho = 4.22\times10^{27}\ \text{m}^{-3}$, the total spin $S = 5\rho V_m/2$ is a huge number and is often much larger than the number of magnons, so that we can safely approximate $S^+ \simeq a\sqrt{2S}$ and $S^- \simeq a^\dagger\sqrt{2S}$ for the low-lying excitations with $\langle a^\dagger a\rangle \ll 2S$ [74]. In this case, the Hamiltonian in Eq. (2) can be rewritten as

$$\begin{aligned} H = {} & \omega_a a^\dagger a + \omega_b b^\dagger b + Ka^\dagger a a^\dagger a + J_0(a + a^\dagger)(b + b^\dagger) \\ & + \Omega(a^\dagger e^{-i\omega_d t} + a e^{i\omega_d t}), \end{aligned} \tag{5}$$

where $\omega_a = \gamma_m B_0 - 2\mu_0 K_{\text{an}}\gamma_m^2 S\hbar/(M^2 V_m)$ is the frequency of the Kittle mode with $\gamma_m/2\pi = 28$ GHz/T, $K = \mu_0 K_{\text{an}}\gamma_m^2\hbar/(M^2 V_m)$ the Kerr nonlinear coefficient, and $J_0 = \sqrt{2S\gamma^2\mu_0\hbar\omega_b/(4V_a)}$ ($\Omega = \sqrt{2S}\mu_0\gamma B_d/4$) the coupling strength between the magnon mode and photon mode (drive field) [74]. Upon rotating the frame with unitary operator $U = e^{-i\omega_d t a^\dagger a}$, the Hamiltonian becomes

$$\begin{aligned} H = {} & \Delta_a a^\dagger a + \omega_b b^\dagger b + J_0(a e^{-i\omega_d t} + a^\dagger e^{i\omega_d t})(b + b^\dagger) \\ & + Ka^\dagger a a^\dagger a + \Omega(a^\dagger + a), \end{aligned} \tag{6}$$

where $\Delta_a = \omega_a - \omega_d$ is detuning between the drive field and the magnon mode. Under a strong driving Eq. (6) can be linearized by rewriting the magnon operator as the expectation value plus its fluctuation, i.e., $a \to \langle a\rangle + a$, leading to the linearized Hamiltonian [75]

$$\begin{aligned} H^{\text{lin}} = {} & \tilde{\Delta}_a a^\dagger a + \omega_b b^\dagger b + J_0(a e^{-i\omega_d t} + a^\dagger e^{i\omega_d t})(b + b^\dagger) \\ & + \tilde{K}(a^\dagger a^\dagger + aa)/2, \end{aligned} \tag{7}$$

where $\tilde{\Delta}_a = \Delta_a + 2K|\langle a\rangle|^2$ and $\tilde{K} = 2K\langle a\rangle^2$. The quadratic terms $a^\dagger a^\dagger$ and aa imply effective self-interaction between magnons induced by magnetocrystalline anisotropy, which may be significantly enhanced by strong driving. In particular, the two quadratic terms are also the key for creating squeezing in nonlinear systems, which can furthermore realize tunable coupling between the magnon mode in the YIG sphere and the photon mode in the superconducting resonator. To show the mechanism, the Hamiltonian (7) can be transferred into the time-dependent squeezed frame determined by the squeezing

operator $S(t) = \exp[r_p(t)(a^{\dagger 2} - a^2)]$ [76] with the squeezing parameter $r_p = (1/2)\arctan(\tilde{K}/\tilde{\Delta}_a)$, the Hamiltonian is composed of the following terms:

$$\begin{aligned} H^s_{\rm unit} &= S^\dagger(t)H(t)S(t) - iS^\dagger(t)\dot{S}(t) + H_{\rm add}, \\ &= H_0 + H_{\rm Rabi} + H_{\rm NA} + H_{\rm add}, \\ H_0 &= \Delta_s a_s^\dagger a_s + \omega_b b^\dagger b, \\ H_{\rm Rabi} &= J_0[(a_s\cosh(r_p) - \sinh(r_p)a_s^\dagger)e^{-iw_d t} \\ &\quad + (a_s^\dagger\cosh(r_p) - \sinh(r_p)a_s)e^{iw_d t}](b + b^\dagger), \\ H_{\rm NA} &= i\dot{r}_p(t)(a^{\dagger 2} - a^2)/2, \\ H_{\rm add} &= -H_{\rm NA}, \end{aligned} \tag{8}$$

where $\Delta_s = \sqrt{\tilde{\Delta}_a^2 - \tilde{K}^2}$. The term $H_{\rm NA}$ describes a nonadiabatic transition induced by mapping the system dynamics into the time-dependent squeezed-light frame. It describes the population transfer between different basis in the squeezed frame. Therefore, we add a term $H_{\rm add} = -i\dot{r}_p(t)(a^{\dagger 2} - a^2)/2$ into the Hamiltonian $H^s_{\rm unit}$ to counteract the nonadiabatic transition. Furthermore, we transform the Hamiltonian (8) into the interaction picture and obtain

$$\begin{aligned} H^I_{\rm unit} &= J_0\cosh r a_s b e^{i\Delta_1 t} + J_0\sinh r a_s^\dagger b e^{i\Delta_2 t} \\ &\quad J_0\cosh r a_s^\dagger b e^{i\Delta_3 t} + J_0\sinh r a_s b e^{i\Delta_4 t} \\ &\quad + \text{H.c.}, \end{aligned} \tag{9}$$

where

$$\begin{aligned} &\Delta_1 = -\omega_d - \Delta_s - \omega_b, \quad \Delta_2 = -\omega_d + \Delta_s - \omega_b, \\ &\Delta_3 = \omega_d + \Delta_s - \omega_b, \quad \Delta_4 = \omega_d - \Delta_s - \omega_b. \end{aligned} \tag{10}$$

By assuming that $\Delta_s = \omega_d + \omega_b$ and neglecting the terms that oscillate with high frequencies $\Delta_{1,3,4}$, the first and last unit cell in the chain can be written as $H^s_{\rm unit} = J_1(a_{1,N}b^\dagger_{1,N} + \text{H.c.})$. As for the remaining unit cells, we arrange alternately two different types of the resonators A_n and B_n in one-dimensional space by interconnecting resonators via the coupler rf SQUID [77–80]. Therefore, the Hamiltonian of the remaining unit cells can be expressed by the quantization process of Eq. (3) as

$$\begin{aligned} H = \sum_{n=2}^{N-1} &(\omega_{a,n}a_n^\dagger a_n + \omega_{b,n}b_n^\dagger b_n + J_1 a_n^\dagger b_n \\ &+ J_2 a_{n+1}^\dagger b_n + \text{H.c.}), \end{aligned} \tag{11}$$

where $\omega_{j,n} = 1/\sqrt{L_{j,n}C_{j,n}}$ $(j = a, b)$ is the oscillator frequency for different types of the resonators A_n and B_n. In addition, the tunable photon-photon coupling between the resonator A_n and the resonator B_n can be written as $J_{1,2} = -\sqrt{\omega_{a,n}/L_{a,n}}\sqrt{\omega_{b,n}/L_{b,n}}(L_0^2)/L(\phi)$, where L_0 is the inductance of the segment shared between resonator and rf SQUID and $L(\phi)$ the effective SQUID inductance with respect to external fluxes $L(\phi) = \partial\phi_{\rm ext}/\partial I_s$ [80]. The flux ϕ threading the SQUID loop gives rise to a circulating current $I_s(\phi) = -I_c\sin(2\pi\phi/\phi_0)$, where ϕ_0 is the flux quantum. Here, ϕ is the sum of the externally applied flux $\phi_{\rm ext}$ and the flux generated by I_s, which can be represented by $\phi = \phi_{\rm ext} + L_s I_s(\phi)$. Thus, the photon-photon coupling can be tunable through adopting controlled voltage pulses generated by an arbitrary waveform generator (AWG) to tune the flux threading rf SQUID loop [81]. After transforming the Hamiltonian (11) into the interaction picture with the unitary transformation $\exp[-it(\sum_n \omega_{a,n}a_n^\dagger a_n + \omega_{b,n}b_n^\dagger b_n)]$, the standard SSH Hamiltonian (1) can be obtained by including the first and last unit cells and the remaining unit cells.

B. SSH model in topologically nontrivial and trivial phases

In order to investigate the topological property in the SSH chain, we set $J_{1,2} = t \pm \delta$ and $t = 1$ is taken as the energy unit. After performing Fourier transformation $S_n = 1/\sqrt{L}\sum_k e^{ikn}S_{k,n}$ with $S = a$ (b), the Hamiltonian can be written as

$$H_I = \psi_k^\dagger h(k)\psi_k, \tag{12}$$

where $\psi_k^\dagger = (a_{k,n}^\dagger, b_{k,n}^\dagger)$ and $h(k) = h_x\sigma_x + h_y\sigma_y$ with σ the Pauli matrix acting on the vector ψ_k, $h_x = (1+\delta) + (1-\delta)\cos k$, and $h_y = (1-\delta)\sin k$. This model belongs to the BDI class according to the standard topological classification [82] and possesses two topological distinct phases for $\delta > 0$ and $\delta < 0$ with the phase transition point at $\delta = 0$, where the gap closes at $k = \pi$. Under the open boundary condition (OBC), the two phases are distinguished by the presence and absence of degenerate zero-mode edge states [83], as shown in Fig. 2(a). Under the periodic boundary condition (PBC), the bulk momentum-space Hamiltonian H_k can be expressed as

$$H_k = \begin{pmatrix} 0 & (1+\delta) + (1-\delta)e^{-ika} \\ (1+\delta) + (1-\delta)e^{ika} & 0 \end{pmatrix}, \tag{13}$$

with $k \in [-\pi/a, \pi/a]$. By solving Eq. (13), we obtain the eigenenergies of the bulk momentum-space Hamiltonian H_k

$$\varepsilon_\pm(k) = \pm\sqrt{(1+\delta)^2 + (1-\delta)^2 + 2(1+\delta)(1-\delta)\cos(ka)}. \tag{14}$$

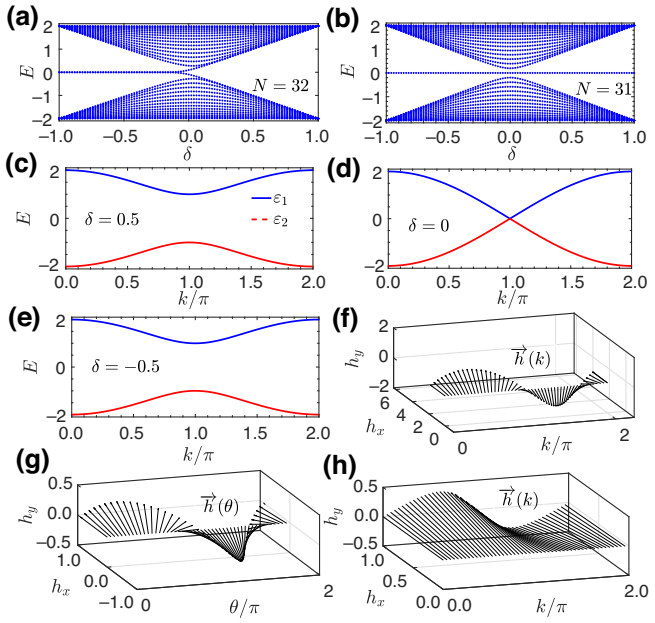

FIG. 2. The spectrum of the SSH model versus δ under OBC for the even size $L = 2N = 32$ of chain in (a) and the odd size $L = 2N - 1 = 31$ in (b). (c)–(e) The spectrum versus k under PBC, with (c) $\delta = -0.5$, (d) $\delta = 0$, and (e) $\delta = 0.5$. The winding number of $h(k)$ across the Brillouin zone in (f),(g), corresponding to (c),(e), respectively. The winding of $h(\theta)$ as θ varies by a period in (g). The arrows in (f)–(h) show the direction of the Hamiltonian $h(k)$ and $h(\theta)$.

The corresponding eigenstates are

$$\varphi_{\pm}(k) = \frac{1}{\sqrt{2}} \begin{pmatrix} e^{-i\phi(k)} \\ \pm 1 \end{pmatrix}, \tag{15}$$

where the phase $\phi(k)$ is given by $\cot\phi(k) = (t + \delta/t - \delta)/\sin ka + \cot ka$. Figures 2(c)–2(e) show the bulk dispersion relations of the SSH model with three different values of δ, including $\delta = -0.5$, 0, and 0.5 in Figs. 2(c)–2(e), respectively.

In Figs. 2(c) and 2(e), there exists a band gap with width $4|\delta|$, which separates the positive eigenenergy band ε_+ from the negative eigenenergy band ε_-. For the case of $\delta = 0$ in Fig. 2(d), the band gap is closed at the first Brillouin zone ($k = \pm\pi$). The SSH chain is more like a "conductor." The band gaps at $\delta > 0$ and $\delta < 0$ are the topological property of the distinct phase, which can be characterized by the Zak phase of the eigenstate $\varphi_-(k)$ [84,85]

$$\mathcal{Z} = i \int_{-\pi}^{\pi} dk [\varphi_-^{\dagger}(k) \partial_k \varphi_-(k)]. \tag{16}$$

Substituting Eq. (15) into Eq. (16), the topological nontrivial (trivial) phase is characterized by $\mathcal{Z} = \pi$ ($\mathcal{Z} = 0$) for $\delta < 0$ ($\delta > 0$). Furthermore, the geometrical meaning of the Zak phase can be known as the winding angle of $h(k)$ as k varies across the Brillouin zone [86], as shown in Figs. 2(a) and 2(c). The direction of $h(k)$ winds an angle of 2π (0) under the condition of $\delta = -0.5$ ($\delta = 0.5$) in the topological nontrivial (trivial) phase. Nevertheless, the Zak phase is ill defined with $\delta = 0$ because of the degeneracy of two bands at $k = \pi$ in Fig. 2(d). In order to trace the topological property of the transition point, the Berry phase on a circle around the gap closing point in the parameter space of $k = A\sin\theta + \pi$ and $\delta = A\cos\theta$, where θ and A are the varying angle and the radius of the circle, respectively. Subsisting these parameters and $\delta = 0$ into $\mathcal{Z}_d = i\int_{-\pi}^{\pi} d\theta[\varphi_-^{\dagger}(\theta)\partial_\theta\varphi_-(\theta)]$, one can obtain $\mathcal{Z}_d = \pi$ for the topological phase transition at $\delta = 0$. In Fig. 2(b), we also show the winding of $h(\theta)$ as θ varies a period, resulting in a winding angle of 2π. In the topologically nontrivial phase with $\delta < 0$, the SSH model for the even size $L = 2N$ maintains robust edge states for an open boundary truncated at the intercell coupling channel [87,88]. However, in the case of odd size $L = 2N - 1$, the right-side end is reduced at the intracell coupling channel and the whole chain is asymmetric. As expected in Fig. 2(b), there is only one topologically protected zero-mode edge state in the band gap with regardless to the value of δ. Therefore, the odd-sized chain always belongs to the topological nontrivial phase [89].

C. Analysis of coupling functions and energy spectrum

In order to realize topologically protected state transfer via zero-mode edge channel in case of a single excitation, we restrict the size of SSH chain to the odd size. Accordingly, the topologically protected zero-mode edge state can be obtained analytically (see Appendix B for details)

$$|\varphi_E\rangle = \sum_{n=1}^{N} (-\lambda)^n a_n^{\dagger} |G\rangle, \tag{17}$$

where $\lambda = J_1/J_2$ and $|G\rangle = |0, 0, 0 \cdots\rangle$ denotes a decoupled state of the magnon-QED-circuit chain with all lattice sites in zero-photon (magnon) Fock state for the middle (endpoint) lattice site. The system can perform a topologically protected state transfer on the zero mode from the left edge to the right edge, corresponding to a single excitation transferring from one side to the other, when setting initially $J_1/J_2 = 0$ while finally $J_1/J_2 = +\infty$. To realize the topologically protected state transfer in an SSH chain, we begin our analysis with the commonly used trigonometric protocol given by [90]

$$\begin{aligned} J_1^{\mathrm{Tri}} &= J_0[1 - \cos(\pi t/T)]/2, \\ J_2^{\mathrm{Tri}} &= J_0[1 + \cos(\pi t/T)]/2, \end{aligned} \tag{18}$$

where T is the total transfer time. In our simulations, we have chosen parameters with practical values that are

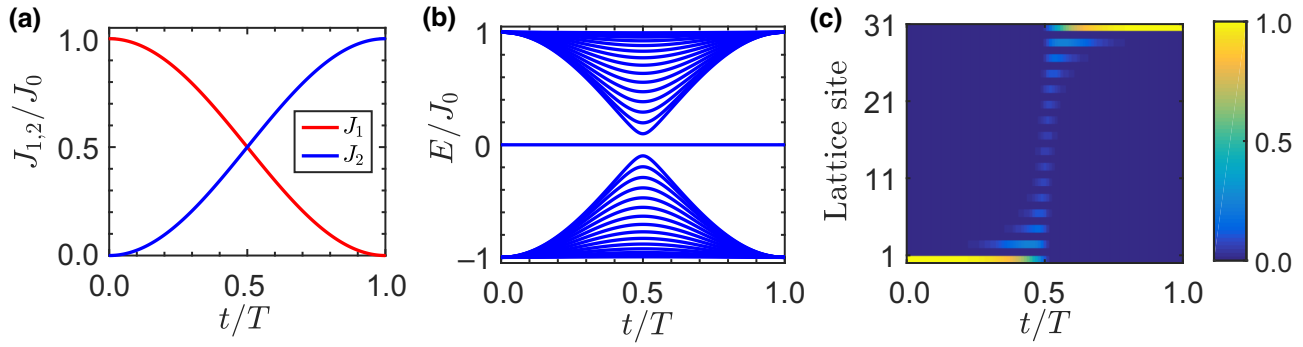

FIG. 3. (a) Functions $J_{1,2}$. (b) The corresponding instantaneous energy spectrum and (c) Distribution of the gap state versus time for the trigonometric protocol. The size of chain is chosen as $L = 2N - 1 = 31$.

experimentally feasible in which we set the bare frequencies of the bosonic modes to be GHZ and the coupling strengths $\max\{J_{1,2}/2\pi\} = J_0/2\pi = 10$ MHz [26,32,46,48,68,91,92]. Accordingly, the ratios between the bare frequencies of the bosonic modes and the coupling strength are approximately equal to 1000. In Figs. 3(a)–3(c), we plot coupling functions for the trigonometric protocol, the corresponding instantaneous energy spectrum and the distribution of gap state versus the transfer time, respectively, by choosing the chain size as $L = 2N - 1 = 31$. Similar to Fig. 2(a), the SSH chain always possesses one zero-mode state keeping unchanged, which is separated from bulk states, shown in Fig. 3(b). The trigonometric protocol results in the topologically protected edge-state transfer that is mainly localized at the first (last) lattice site at the beginning (end) instant in the odd-sized SSH chain, seen from the brightest fringes in Fig. 3(c).

The above state-transfer process needs to satisfy the adiabatic limit [62,65,90]. A sufficient condition for the adiabatic evolution is $\Delta E = |E_m(t) - E_n(t)| \gg |\langle\dot{\varphi}_m(t)|\varphi_n(t)\rangle|$, where E_m, E_n, $|\varphi_m(t)\rangle$, and $|\varphi_n(t)\rangle$ are the mth and nth instantaneous eigenenergies and corresponding eigenstates of the Hamiltonian, and the overdot indicates differentiation with respect to time. For the sake of satisfying the adiabatic limit, the time evolution of the adiabatic state transfer should be very slow to make the evolution remain in the zero mode (edge state) without exciting other eigenstates (bulk states) due to a trivial ΔE. The adiabatic limit condition can be relaxed to realize fast topological transfer by tailoring the eigenenergy difference ΔE properly to form a nontrivial band gap in the Hamiltonian spectrum or/and decreasing the derivative of the Hamiltonian. As a consequence, it is crucial to suitably design the coupling functions by relaxing the adiabatic limit. Here we specify that the couplings are shaped by a linear function [65]

$$\begin{aligned} J_1^{\text{Lin}} &= J_0 t/T, \\ J_2^{\text{Lin}} &= J_0[1 - t/T], \end{aligned} \tag{19}$$

the tangential protocol [93]

$$\begin{aligned} J_1^{\text{Tan}} &= J_0[\tan(-\pi t/T_f - \nu)/2(\tan\nu + 1)], \\ J_2^{\text{Tan}} &= J_0[\tan(\pi t/T_f + \nu)/2(\tan\nu + 1)], \end{aligned} \tag{20}$$

with $T_f = \pi T/(2\pi - 2\nu)$ and $\alpha = \pi/2 + 0.4$, and the three-step protocol

$$\begin{aligned} J_1^{\text{3-step}} &= \begin{cases} \dfrac{20J_0 t}{9T} & t \le 0.45T \\ J_0 & 0.45T < t \le T, \end{cases} \\ J_2^{\text{3-step}} &= \begin{cases} J_0 & t \le 0.55T \\ \dfrac{20J_0}{9}(1 - \dfrac{t}{T}) & 0.55T < t \le T. \end{cases} \end{aligned} \tag{21}$$

These three forms of $J_{1,2}$ in Eqs. (19) and (20) satisfy the single-excitation state-transfer conditions $\lambda|_{t=0} = 0$ and $\lambda|_{t=T} = +\infty$ well.

In Fig. 4, we plot each protocol for the coupling functions in the left panel and the corresponding instantaneous energy spectrum in the right, respectively, with the linear protocol in Figs. 4(a) and 4(b), the tangential protocol in Figs. 4(c) and 4(d), and the three-step protocol in Figs. 4(e) and 4(f). These protocols are similar in that the energy gap between the edge state and the bulk state reaches at the maximum value at the initial and final instants while the energy gap tends to the minimum value at $J_1 = J_2$. Nevertheless, the coupling functions in those protocols approach the minimum value of the energy gap by different slopes. In Figs. 3(a) and 3(b), the trigonometric protocol drives the system more slowly (faster) in the beginning and in the end (in the middle time), while in Figs. 4(a) and 4(b) the linear protocol approaches and departs from the closed gap point at the same rate. As for the tangential protocol shown in Figs. 4(c) and 4(d), the coupling functions are designed in a direction opposite to that of the trigonometric protocol, which drives the system approaching rather slowly the closed gap point and staying longer in its vicinity. All aforementioned schemes have the property of $J_1(t) +$

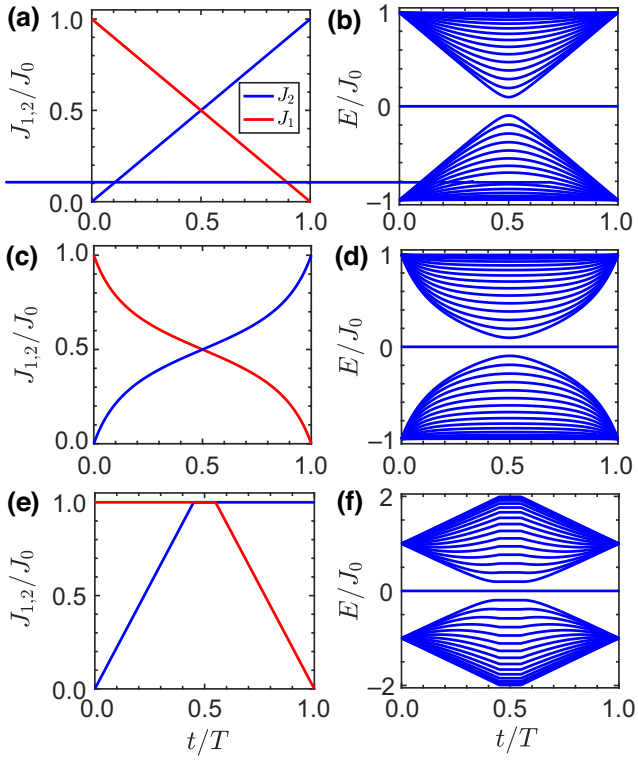

FIG. 4. Functions $J_{1,2}$ and corresponding instantaneous energy spectra versus time for the linear protocol in (a),(b), the tangential protocol in (c),(d), the three-step protocol in (e),(f). The size of chain is chosen as $L = 2N - 1 = 31$.

$J_2(t) = J_0$ for each instant t, resulting in the maximum of energy $E_{\max} = J_0$ in Figs. 3(b), 4(b), and 4(d). In particular, the three-step protocol exhibits $J_1(t) + J_2(t) \geq J_0$ during the whole process, which is bounded by $J_{1,2}(t) \leq J_1(0)$ or $J_{1,2}(t) \leq J_2(T)$ for each instant t of the process. As shown in Fig. 4(e), the couplings keep in the mirror symmetry, including three intervals: (i) the coupling J_1 remains constant to the maximum value and the coupling J_2 increases linearly to this value with a larger slope comparing to the linear protocol; (ii) both couplings $J_{1,2}$ are equal to the maximum value; and (iii) the coupling J_1 falls linearly and the other keeps constant at the maximum value. Figure 4(f) shows that the maximum value of energy $E_{\max} = 2J_0$ stays at the vicinity of the closed gap at the interval of $t/T \in [0.45, 0.55]$.

According to time-dependent coupling functions in the linear protocol, the tangential protocol and the three-step protocol, we plot the state distribution of the gap state versus transfer time in Figs. 5(a)–5(c). Similar to the analytical calculation in Eq. (17), the zero-mode state is localized at the first (last) site and the distribution of left (right) edge state with zero mode is equal to unity at the beginning (end) instant to realize the topologically protected edge-state transfer with protocols in Figs. 5(a)–5(c). However, as shown by bright fringes in Figs. 5(a)–5(c), the distribution of the gap state at odd sites are enlarged in the time scale compared with Fig. 3(c), which indicates the nonadiabatic transitions among the edge state and bulk states are more obvious. In other words, the linear, the tangential, the three-step functions approach and depart from the closed gap point at a larger rate than the trigonometric functions, resulting in a higher probability of nonadiabatic excitations when the gap closes.

III. FAST MAGNON-MAGNON TRANSFER

A. Single-excitation magnon-magnon transfer

In the following, we focus on the quantitative difference of the topologically protected edge-state transfer based on different protocols. Concretely, when the initial state is prepared in the magnonic left edge state $|l\rangle = |1, 0, 0, \ldots, 0, 0\rangle_L$, the magnonic right edge state $|r\rangle = |0, 0, 0, \ldots, 0, 1\rangle_L$ can be obtained through the evolution via the protected edge channel. In Fig. 6(a), we take $L = 31$ as an example to plot the final fidelity $F(T)$ of the state-transfer process as a function of the total transfer time T based on different protocols. The fidelity can be defined as $F(t) = \langle r|\rho(t)|r\rangle$, where $|r\rangle$ and $\rho(t)$ are the target state and the time-dependent density matrix of the system by solving Liouville equation $\dot{\rho}(t) = -i[H_I, \rho]$, and t corresponds to the evolution instant. In particular, we set a lower bound in fidelity and consider the final time at which the fidelity is 0.99. In Fig. 6(a), for all protocols, the fidelity tends to unity in the limit of $T \to +\infty$, meaning the complete magnon-magnon transfer of the single excitation along the chain. In particular, the trigonometric protocol, the linear protocol and the tangential protocols have smoothly increasing fidelity with the transfer time and reaches $F(T) > 0.99$ for the total time $T_{\text{trig}} = 1244/J_0$, $T_{\text{linear}} = 803/J_0$, and $T_{\text{tan}} = 197/J_0$, respectively. The fidelity of three-step protocol with the total transfer time has the oscillating behavior, as expected from the relatively long time spent near the closed gap. This oscillating behavior stems from the resonant interaction between the zero-mode edge state and the bulk state, which can shorten the total transfer time significantly in comparison to a completely adiabatic process of the trigonometric protocol, the linear protocol and the tangential, and the exponential protocols [65]. However, the first peak reaches the target fidelity $F_{3\text{-step}} = 0.996$ at time $T_{3\text{-step}} = 71/J_0$. Thus, the three-step protocol demands a relative higher precision when tuning the total transfer time but increases the evolution efficiency significantly, which is almost 17 times shorter than the trigonometric protocol.

Accordingly, in order to more intuitively reflect the speed of completing, different sizes of chain L and corresponding evolution times of the magnon-magnon transfer reaching the fidelity of $F = 0.99$ are chosen as numerical samples to fit the function of the total transfer time T versus L in Fig. 6(b). The fitting functions

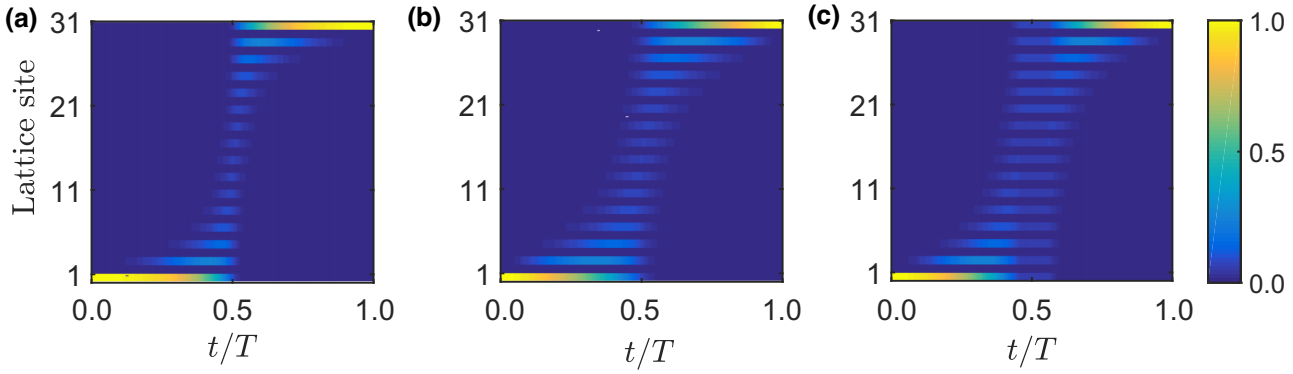

FIG. 5. Distribution of the gap state versus transfer time for the the linear protocol in (a), the tangential protocol in (b) and the three-step protocol in (c). The size of chain is chosen as $L = 2N - 1 = 31$.

for the four protocols are $J_0 T_{\text{trig}} = 1.197L^2 + 5.158L - 61.31$, $J_0 T_{\text{linear}} = 0.7819L^2 - 0.493L + 28.98$, $J_0 T_{\text{tan}} = 0.1889L^2 + 0.6916L - 8.406$, and $J_0 T_{3\text{-step}} = 0.006002L^2 + 2.629L - 19.25$, respectively. As L increases, the total time of magnon-magnon transfer shows a quadratic trend with L for all protocols. For example, in order to realize magnon-magnon transfer along the size of chain $L = 81$, the fidelity with $F(T) = 0.99$ demands the total transfer time $T_{\text{trig}}^{L=81} \approx 130.7$ μs, $T_{\text{linear}}^{L=81} \approx 81.47$ μs, $T_{\text{tan}}^{L=81} \approx 20.48$ μs, $T_{3\text{-step}}^{L=81} \approx 3.710$ μs by choosing the value of $J_0 = 2\pi \times 10$ MHz [32,45,48,94–96]. It is evident that the efficiency of evolution based on the three-step protocol improves more significantly with a larger N than the linear protocol, the tangential protocol and the trigonometric protocol.

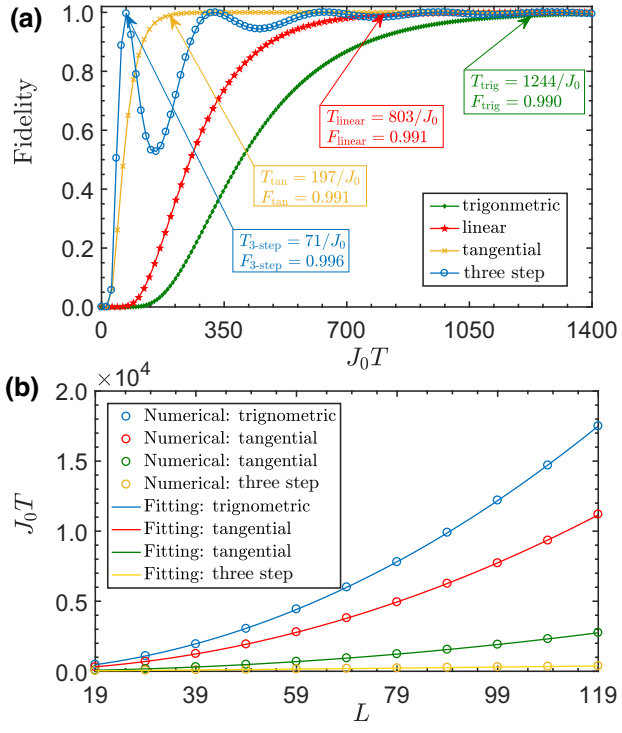

FIG. 6. (a) Final fidelity of magnon-magnon transfer of the single excitation for $|1,0,0,\ldots,0,0\rangle_{31}$ and $|0,0,0,\ldots,0,1\rangle_{31}$ as a function of the total transfer time for different protocols. The size of chain is chosen as $L = 2N - 1 = 31$. (b) Fitting functions and numerical scatters between the size of chain and total transfer time with 99% fidelity for the trignometric protocol, linear protocol, tangential protocol and three-step protocol.

Fast quasiadiabatic and related approaches depart from the core of paradigms discussed so far in that they are intended from the start as approximate methods to balance two conflicting aims: shortening the process time and keeping the process as adiabatic as possible with respect to the actual Hamiltonian. The difference between the two schemes the three-step scheme used here and the existing exponential scheme [65] lies in the form of designing coupling functions $J_{1,2}$, which determines the rate of varying the Hamiltonian during the evolution of the system. In order to satisfy the adiabatic limit, a sufficient condition is $\sum_{m\neq n}(\langle\psi_n(t)|\partial H(t)/\partial t|\psi_m(t)\rangle)/(|E_m(t) - E_n(t)|) \ll 1$, where $E_{n,m}$ and $|\psi_{n,m}(t)\rangle$ are the nth and mth eigenenergies and corresponding eigenstates obeying the instantaneous eigenequation $H(t)|\psi_n(t)\rangle = E_n(t)|\psi_n(t)\rangle$. Generally, the energy gap between the channel and bulk states is quite small, thus the system should be driven slowly enough to make the initial state evolve along the channel state without exciting bulk states. The strategy is to distribute its rate of designing the maximum value of the coupling functions and the corresponding appropriate slopes so that adiabatic process can be sped up and diabatic transitions are equally likely along the process. Therefore, the most essential difference between the three-step protocol and the exponential protocol [65] is that small coherent dynamics exists in the three-step protocol, which is further shortened the evolution time of the topologically protected QST. The import of the small coherent dynamics leads to a "special point" for $T_{3\text{-step}} = 71/J_0$ with $L = 31$ in Fig. 6(a), which is intrinsically different from the smooth exponential coupling functions obtained by the CRAB algorithm [65]. At this special point, the fidelity of QST

employing by the three-step protocol cannot reach only 0.99 but also the evolution time is greatly shortened than the exponential protocol.

B. Multiexcitation magnon-magnon transfer

In this section, we discuss the multiexcitation magnon-magnon state transfer in the magnon-QED-circuit model. In order to explain the case that multiexcitation magnon-magnon state transfer can be realized in the SSH model, we expand the Hamiltonian in the form of matrix product

$$H_{\text{matri}} = \left(a_1^\dagger, b_1^\dagger, a_2^\dagger, b_2^\dagger, \ldots, a_{N-1}^\dagger, b_{N-1}^\dagger, a_N^\dagger\right) \times \begin{pmatrix} 0 & J_1 & 0 & 0 & \cdots & 0 & 0 & 0 \\ J_1 & 0 & J_2 & 0 & \cdots & 0 & 0 & 0 \\ 0 & J_2 & J_1 & 0 & \cdots & 0 & 0 & 0 \\ 0 & 0 & J_1 & 0 & \cdots & 0 & 0 & 0 \\ \cdots & \cdots & \cdots & \cdots & \cdots & \cdots & \cdots & \cdots \\ 0 & 0 & 0 & 0 & \cdots & 0 & J_2 & 0 \\ 0 & 0 & 0 & 0 & \cdots & J_2 & 0 & J_1 \\ 0 & 0 & 0 & 0 & \cdots & 0 & J_1 & 0 \end{pmatrix} \times \begin{pmatrix} a_1 \\ b_1 \\ a_2 \\ b_2 \\ \vdots \\ a_{N-1} \\ b_{N-1} \\ a_N \end{pmatrix}. \tag{22}$$

In order to realize the multiexcitation magnon-magnon transfer, the initial state of the system is prepared in the magnonic left edge state, which can be expressed as

$$\begin{aligned} |l\rangle_{\text{multi}} &= \frac{(a_1^\dagger)^n}{\sqrt{n!}}|0,0,0,\ldots,0,0\rangle_L \\ &= |M,0,0,\ldots,0,0\rangle_L, \end{aligned} \tag{23}$$

where $M = \langle a_n^\dagger a_n\rangle$ is the total excitation number in the magnon. Going through the topologically protected evolution, the multiexcitation particle in the magnon can be absorbed to evolve into the magnonic right edge state, which can be written as

$$\begin{aligned} |r\rangle_{\text{multi}} &= \frac{(a_N^\dagger)^n}{\sqrt{n!}}|0,0,0,\ldots,0,0\rangle_L \\ &= |0,0,0,\ldots,0,M\rangle_L. \end{aligned} \tag{24}$$

As an example with the full Hamiltonian Eq. (22), we numerically plot the final excitation number in Fig. 7(a), when the initial state is prepared as the left magnonic state $|l\rangle_{\text{multi}} = |M,0,0,0,0\rangle_5$ $(M = 2,3,4)$ by choosing the size of chain $L = 5$ and employing the three-step protocol. Figure 7(a) shows that the excitation number $M = \langle a_3^\dagger a_3\rangle$ tends to their maximum value of excitation number in the limit of $J_0T \to 100$ for $M = 2, 3$, and 4, respectively.

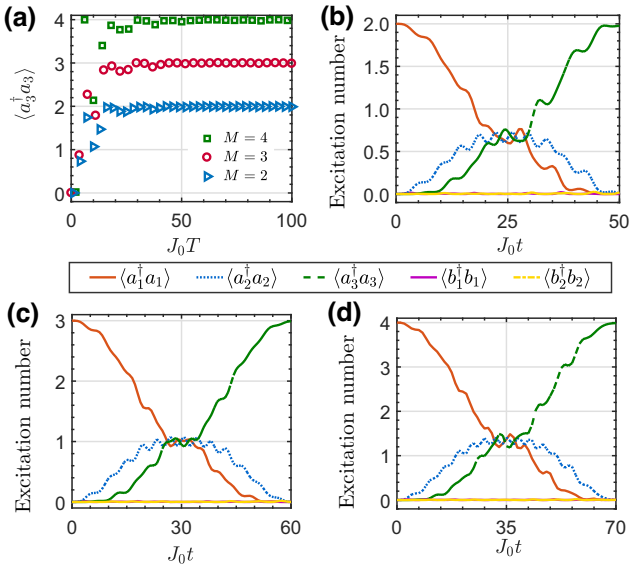

FIG. 7. (a) Final excitation number of multiexcitation magnon-magnon transfer as a function of the total transfer time by employed the three-step protocol. (b)–(d) Time evolutions of the excitation number for each lattice site in the case of multiexcitation magnon-magnon transfer for $|l\rangle_{\text{multi}} = |M,0,0,0,0\rangle_5$ and $|r\rangle_{\text{multi}} = |0,0,0,0,M\rangle_5$ for $M = 2$ in (b), $M = 3$ in (c), and $M = 4$ in (d), respectively, by employed the three-step protocol. The size of chain is chosen as $L = 2N - 1 = 5$.

Next, we plot the time evolutions of excitation number for each lattice site in the case of multiexcitation magnon-magnon transfer by choosing different excitation number $M = 2$ in Fig. 7(b), $M = 3$ in Fig. 7(c), and $M = 4$ in Fig. 7(d), respectively. The excitation number of the first (last) site A_1 (A_3) evolves from the maximum (minimum) value into the minimum (maximum) value at the beginning and the end of the evolution time shown by the red line and green dashed line, which indicates that the multiexcitation magnon-magnon transfer $|l\rangle_{\text{multi}} = |M,0,0,0,0,0\rangle_5 \to |r\rangle_{\text{multi}} = |0,0,0,0,M\rangle_5$ can be realized successfully by employing the three-step protocol. Therefore, it is proved that multiexcitation magnon-magnon state transfer can also be realized in the proposed photon-mediated SSH model by a fast topologically protected process. Also, it is straightforward to conclude that a transfer of arbitrary superposed state (or a mixed state) of magnon can be achieved.

IV. ROBUSTNESS AND SCALABILITY

The one-dimensional magnon-QED-circuit chain may contain imperfection resulting in the nonideal SSH model,

due to the process of the erroneous physical implementation, experiment equipment, and operations, which could destroy the perfect magnon-magnon transfer. It is necessary to analyze the influence of imperfect factors on the magnon-magnon transfer based on those protocols. Concretely, we consider three dominant aspects of influence in the ideal SSH chain: (i) unwanted on-site potential defects for YIG spheres and resonators from external magnetic field for the imperfect magnetization of YIG spheres and from the mutual inductance and self-inductance of circuit for the defective quantization of the LC resonators; (ii) inevitable variation in ideal couplings from the unstable magnetic flux threading to the SQUID loops and from direct crosstalk between static and driving magnetic fields applying on the YIG spheres; (iii) losses of photon in the odd lattice sites and magnon in the endpoint lattice sites with decay rate γ_n, and losses of photon in the even lattice sites with decay rates κ_n.

Considering on-site potential defects and the variation of ideal couplings, the chain can be described by

$$H_d = \sum_{n=1}^{N} w_{a,n} a_n^\dagger a_n + \sum_{n=1}^{N-1} w_{b,n} b_n^\dagger b_n + \sum_{n=1}^{N-1} \left(J_1^{'} a_n^\dagger b_n + J_2^{'} a_{n+1}^\dagger b_n + \text{H.c.} \right), \tag{25}$$

with $J_{1,2}^{'} = J_{1,2} + \text{rand}[-\delta_{J_{1,2}}, \delta_{J_{1,2}}]$, $w_{a(b),n}$ being the strength of on-site potential defect for odd lattice site A_n (even lattice site B_n), $w_{a(b),n} = \text{rand}[-w_{a(b),n}, w_{a(b),n}]$, and $\text{rand}[-x, x]$ indicating a uniformly distributed random number in the range of $[-x, x]$. Here, we choose the disorder strengths of on-site potential defects and couplings as $w_{a(b),n} = \delta_{J_{1,2},n} = \Delta$ as an example. The relations between the magnon-magnon transfer fidelity and the disorder of coupling strengths and of on-site potential defects are shown in Figs. 8(a) and 8(b), respectively. The disorder is randomly sampled 10^4 times so that the fidelity is taken as an average of the 10^4 results versus the disorder. When comparing with the disorder in unexpected couplings and on-site potentials based on those protocols, it is found that the magnon-magnon transfer fidelities hold relatively great robustness to the variation of couplings, while the on-site potential defects destroy the transfer process more distinctly, because the chiral symmetry of the SSH model is unbroken (broken) by a small value of disorder in unexpected couplings (on-site potentials) [89].

Nevertheless, by inspecting Fig. 8(a), all protocol are relatively insensitive to the disorder in unexpected couplings apart from the three-step protocol. When $\Delta = 0.5$, the fidelity of the three-step protocol drops to around 0.8 rather than reaching above 0.96 for other protocols. On the other hand, when considering the effect of on-site potential defects for all sites in Fig. 8(b), the transfer fidelity of the tangential protocol is affected by the disorder minimally. As for the linear protocol and the trigonometric

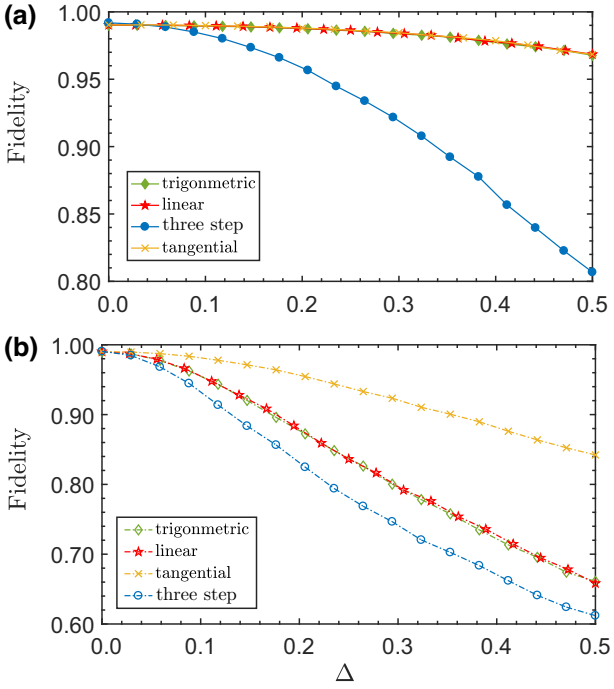

FIG. 8. Final fidelity of state transfer for all protocols against (a) the unexpected coupling strength and (b) the on-site potential defect for all lattice sites with disorder Δ. The size of chain is chosen as $L = 2N - 1 = 31$.

protocol, the magnon-magnon transfer fidelities have the same decline trend with increasing Δ. Still, the three-step protocol is susceptible to the disorder of on-site potential defects, whose transfer fidelity is damaged by around 40% when $\Delta = 0.5$. In the existence of whether unexpected coupling defects or on-site potential defects among all protocols, the numerical results prove that the three-step protocol and the tangential protocol render the poorest and greatest robustness against the disorders, respectively. It is no wonder that the improvement of the three-step protocol in speed relies on the consumption of robustness against disorder because of the fast evolution process and the large average value of coupling strengths for each instant. As shown in Fig. 9, we plot the fidelity of magnon-magnon transfer versus the varying disorder strength Δ of coupling strength and the total evolution time $J_0 T$ by the three-step protocol for $L = 31$ and $L = 57$. We can learn that the damage to fidelity caused by coupling defects can be compensated by specific evolution time regions of $J_0 T \in [55, 89] \cup [254, 400]$ for $L = 31$ and $J_0 T \in [130, 187] \cup [551, 700]$ for $L = 57$, respectively. In particular, the regions with a $F > 0.90$ fidelity are consistent with the evolution time of "special point" in Fig. 6(a) indicating that the damage from fluctuations of coupling functions on the transfer fidelity can be compensated by modulating the evolution time to "special

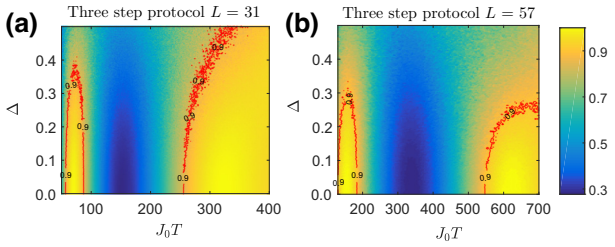

FIG. 9. The fidelity of the magnon-magnon transfer versus the varying disorder strength Δ of coupling strength and the total evolution time J_0T by the three-step protocol for $L = 31$ in (a) and for $L = 57$ in (b).

points" in the three-step protocol. From the above numerical results, the linear, the trigonometric, the tangential, and the exponential [65] protocols depend on a completely adiabatic transfer process limited by adiabatic condition strictly in the Hamiltonian to suppress the resonant process. In respect to the three-step protocol, the appropriate resonant process can be properly handled to increase the efficiency of the transfer process, which leads to the fact that the partial sacrifice of robustness against on-site potential defects and unexpected coupling defects significantly improves the robustness against effects of losses on the transfer efficiency.

When considering the case of two dominant lossy channels for magnons and photons, the dynamics of system can be governed by the Markovian master equation

$$\partial_t \rho = i[\rho, H_I] + \sum_{n=1}^{N} \kappa_n \pounds[a_n] + \sum_{n=1}^{N-1} \gamma_n \pounds[b_n], \tag{26}$$

where $\pounds[a_n] = a_n \rho a_n^\dagger - a_n^\dagger a_n \rho/2 - \rho a_n^\dagger a_n/2$ and $\pounds[b_n] = b_n \rho b_n^\dagger - b_n^\dagger b_n \rho/2 - \rho b_n^\dagger b_n/2$. For convenience, we assume that $\kappa_n = \kappa$, $\gamma_n = \gamma$ and $J_0/2\pi = 10$ MHz. Figures 10(a)–10(d) demonstrate the relation between the fidelity and decay rates of photon (magnon) in the odd (endpoint) lattice sites and photon in the even lattice sites for the trigonometric protocol, the linear protocol, the tangential protocol and the three-step protocol, respectively. All protocols exhibit great robustness to the decay rate of photon and magnon in the odd lattice sites, which are sensitive to the decay rate of photon in the even lattice sites, due to the virtual excitation of photon in the resonator B_n during the whole magnon-magnon transfer process. As the decay rate of photon and magnon in the odd lattice sites and photon in the even lattice sites increases, transfer fidelities of all protocols show a evident or slight trend of decline, respectively. The reason lies in the interaction property of the system, that is, the formulation of the Hamiltonian, which determines that the distribution of zero-mode state of system on different lattice sites. In the SSH model,

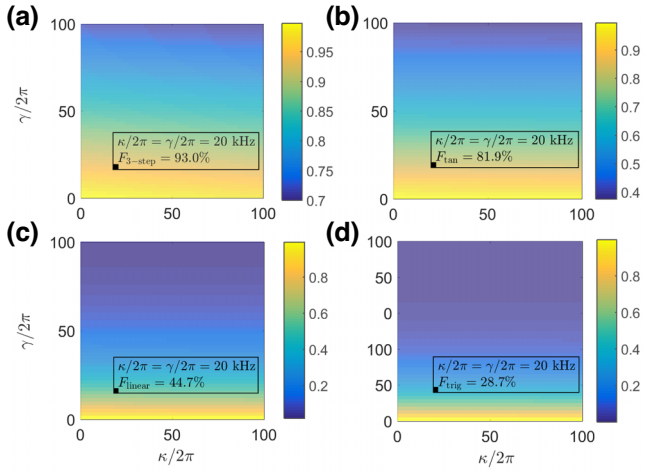

FIG. 10. Effects of losses on the final fidelity of state transfer for the trignometric protocol, linear protocol, tangential protocol and 3-step protocol. We choose $J_0/2\pi = 10$ MHz, the corresponding total transfer time $T_{\text{trig}}^{L=31} = 19.80$ μs, $T_{\text{linear}}^{L=31} = 12.64$ μs, $T_{\text{tan}}^{L=31} = 3.10$ μs and $T_{3\text{-step}}^{L=31} = 1.07$ μs with a 99.9% fidelity of the magnon-magnon transfer.

according to $H_{2N-1}|\phi_E\rangle = 0$, one can calculate the analytic form of the zero-mode state of the system in Eq. (17) (see Appendix B), for which it is exactly one of the most relevant features of the SSH model that zero-mode state only distributes on odd-size lattice sites while involves no even-size ones [9,97,98]. Furthermore, this feature can be also embodied in the distribution of the gap state, which increases exponentially on the odd sites while exhibits no distribution on the even sites, seen from the the bright yellow and dark blue fringes in Fig. 4. Thus, all protocols exhibit the great robustness to the decay rate of photon in the even lattice sites while are sensitive to the decay rate of photon in the odd lattice sites and of magnon in the endpoint lattice sites, because the excitation is virtual for photon in the resonator B_n but real for magnon in the YIG sphere $A_{1,N}$ and for photon in the resonator A_n.

Comparing with the trigonometric protocol, the fidelities of other protocols have been enhanced to different degrees depending on the total transfer time, in particular, for the tangential protocol and the three-step protocol. Accordingly, the fidelity of magnon-magnon transfer along the chain with the size of $L = 31$ can reach $F_{3\text{-step}} = 93\%$, $F_{\text{tan}} = 81.9\%$, $F_{\text{linear}} = 44.7\%$, and $F_{\text{trig}} = 28.7\%$, respectively, under an experimentally feasible condition of $\kappa/2\pi = \gamma/2\pi = 20$ kHz [32,48,96,99,100]. The above results manifest the tangential and the three-step protocols enhance robustness largely against losses of the system. Furthermore, we focus on the scalability of magnon-magnon transfer based on different protocols, which is another crucial direction to verify the efficiency of a QST protocol. As a consequence, the import of coherent dynamics in the three-step scheme not only greatly reduces

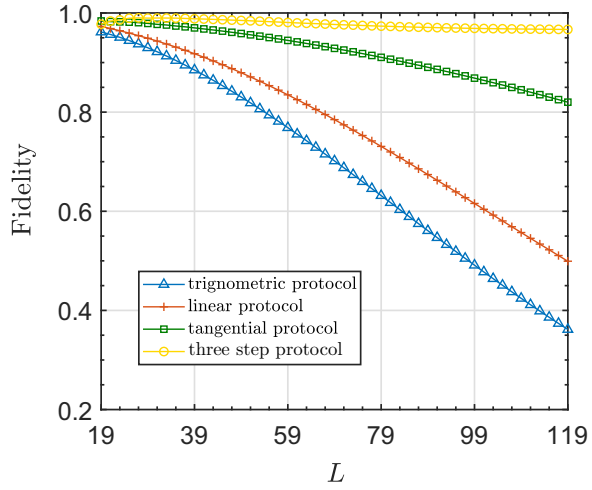

FIG. 11. Final fidelities of state transfer with the scalability L under the coupling strength $J_0/2\pi = 10$ MHz and decay rates of photon and magnon in the odd lattice sites and of photon in the even lattice sites (e.g., $\gamma/2\pi = \kappa/2\pi = 20$ kHz) for the trignometric protocol, linear protocol, tangential protocol, and three-step protocol.

the evolution time, but also weakens the damage of the state-transfer fidelity caused by the losses of system.

In Fig. 11, we plot final fidelities of magnon-magnon transfer versus the scalability L. It is assumed that the lossy system is employed with the coupling strengths $J_0/2\pi = 10$ MHz and the experimentally feasible decay rates of magnons and photons are fixed with $\gamma/2\pi = \kappa/2\pi = 20$ kHz [32,48,96,99,100]. It is evident that the fidelity declines with increasing L for all protocols. With regard to the scalability $L = 119$, the fidelities of magnon-magnon transfer in the tangential protocol and the three-step protocol can be maintained over 80% and 90%, respectively. Moreover, the three-step protocol and the tangential protocol show greater superiority in the aspect of the scalability than the other protocols with increasing L. It can be found that the three-step protocol can be employed in different system situations. In the first case, the hybrid system designed for magnon-magnon state transfer is vulnerable to external perturbations of coupling functions and on-site potential defects. However, we can increase the evolution time to resist imperfect parameters on the QST fidelity by balancing evolution speed and parameter robustness. In the second case, if the losses of system or/and the size of SSH chain are large, "special points" can be selected in the three-step protocol to reduce effect of the lossy channels for magnons and photons on the QST fidelity.

V. DIFFERENT KINDS OF CONTROLLABLE SINGLE-EXCITATION TRANSFERS

In this section, we now discuss different kinds of controllable QSTs in the magnon-QED-circuit chain, which is induced by the corresponding defect strength on different types of lattice sites in the two ends. For convenience, the 3-step protocol is employed by the following defect-induced controllable quantum transfer in case of the single excitation.

A. Magnon-photon and photon-magnon transfers

Still based on the odd-sized SSH chain of realizing the magnon-photon and photon-magnon transfers with diagrammatic sketches Figs. 12(a) and 12(b), respectively, the constant on-site potential defects are imposed on the specific lattice site, e.g., the first lattice cell for YIG sphere A_1 and the penultimate lattice cell for superconducting resonator B_{N-1}, and the first lattice cell for superconducting resonator B_2 and the last lattice cell for YIG sphere A_N. In our setup, a local NbTi superconducting coil generates the coil magnetic field onto the nearby YIG sphere and the value of inductance and capacitance can be allowed for the individual magnon and photon frequencies control, respectively, as shown in Fig. 1(b). The corresponding full Hamiltonian can be written as

$$H_{\text{full}} = \sum_{i,j}(w_{a,i}a_i^\dagger a_i + w_{b,j}b_j^\dagger b_j) + \sum_{n=1}^{N-1}\big(J_1 a_n^\dagger b_n + J_2 a_{n+1}^\dagger b_n\big) + \text{H.c.}, \tag{27}$$

where $\{i = 1, j = N-1\}$ and $\{i = N, j = 1\}$ indicate the conditions of defect lattice cell to realize the magnon-photon and photon-magnon transfers, respectively. For convenience, we suppose that the defect strengths of on-site potentials are imposed equally by setting $w_{a(b),i(j)} = w = 12J_0$.

In order to realize photon-magnon and magnon-photon transfers, the energy spectra of defect SSH chains become irregular, which are embodied by two energy states separating from the bulk state close to the zero-mode edge state and two far larger energy states, as shown in Figs. 13(a) and 13(e), respectively. The corresponding photon-magnon and magnon-photon transfer distributions of the gap state close to the initial and end instants are shown in Figs. 13(b) and 13(c), and in (c) and (h), respectively. The distribution reveals that the edge state is mainly localized in the last (penultimate) lattice site B_{30} (A_{31}) at the initial time $t = 0.05T$, and the second (first) lattice site B_1 (A_1) at the end time $t = 0.95T$, respectively, with regard to the magnon-photon (photon-magnon) transfer process. It highlights to us that the magnon-photon and photon-magnon transfers can be realized by the processes of $|0,0,0,\ldots,0,1\rangle_{31} \longrightarrow |0,1,0,\ldots,0,0\rangle_{31}$ and $|0,0,0,\ldots,1,0\rangle_{31} \longrightarrow |1,0,0,\ldots,0,0\rangle_{31}$, respectively. To further verify the defect-induced controllable transfer processes, we use time-dependent full Hamiltonian (27) to evolve the initial states prepared in $|0,0,0,\ldots,0,1\rangle_{31}$

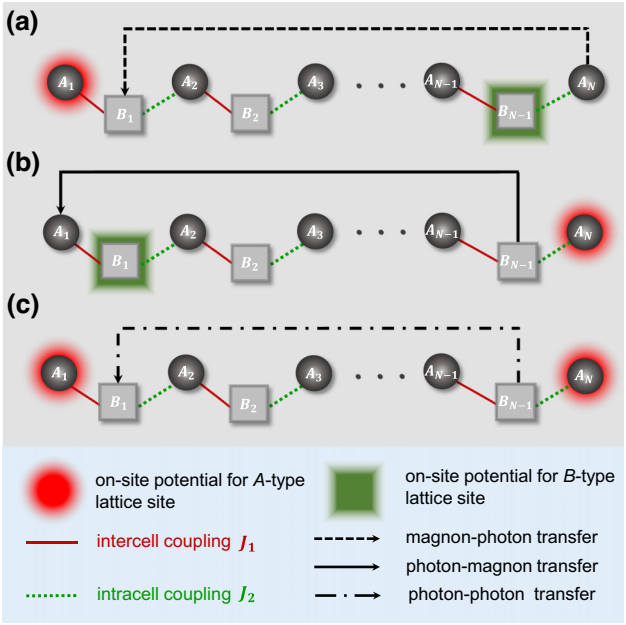

FIG. 12. The diagrammatic sketches of the YIG sphere-superconducting resonator and odd-sized SSH model with the various on-site potential defects to realize (a) the magnon-photon transfer imposed by the first and penultimate lattice site with on-site potential defects, (b) the photon-magnon transfer imposed by the second and last lattice site with on-site potential defects, and (c) the photon-photon transfer imposed by the second and penultimate lattice site with on-site potential defects. The relevant information is shown in the blue shaded area.

and $|0,0,0,\ldots,1,0\rangle_{31}$, respectively, by solving Liouville equation. In Figs. 13(d) and 13(h), the near-unity distribution at the begin and the end transfer time indicates the successes of defect-induced magnon-photon and photon-magnon transfers.

In order to more intuitively reflect the essence of the magnon-photon and photon-magnon transfers, the effective Hamiltonian of the magnon-QED-circuit chain with specific on-site potential defects can be derived as, respectively (see Appendix C for details),

$$\begin{aligned} H_{\text{eff}}^{mp} &= J_{\text{eff}}^{mp} a_{N-1}^{\dagger} a_N + \sum_{n=2}^{N-2} J_1 a_n^{\dagger} b_n + \sum_{n=1}^{N-2} J_2 a_{n+1}^{\dagger} b_n \\ &\quad + \text{H.c.}, \\ H_{\text{eff}}^{pm} &= J_{\text{eff}}^{pm} a_1^{\dagger} a_3 + \sum_{n=2}^{N-1} J_1 a_n^{\dagger} b_n + \sum_{n=2}^{N-2} J_2 a_{n+1}^{\dagger} b_n \\ &\quad + \text{H.c.}, \end{aligned} \tag{28}$$

where $J_{\text{eff}}^{mp(pm)} = J_1 J_2 / w_{b,N-1(1)}$. The effective Hamiltonian excludes the first lattice site A_1 and the last lattice site A_N for the magnon-photon and photon-magnon transfers, respectively. The above defect-induced controllable transfer is required with relative large value of on-site potential defect strength in specific lattice sites and the relevant initial state, which is the key point to realize the defect-induced controllable transfer.

B. Defect-induced photon-photon transfer

Taking the head and the tail on-site potential defects into account in the magnon-QED-circuit chain shown in Fig. 9(c), The energy spectrum of defect SSH chain with the first and last on-site potential defects shown in Fig. 14(a) has the similar energy spectrum with the standard SSH chain in Fig. 3(h), except for two larger value energy states separating from the bulk states and edge state. Comparing with the defect-induced magnon-photon and photon-magnon transfer, it is no wonder that the topologically protected edge state still keeps the greater separation from the bulk states during the whole transfer time, where there exists only an insignificant energy shift for the edge state. Accordingly, the distributions of the gap state are at the initial and end instants demonstrated in Figs. 14(b) and 14(d), respectively. It is evident that the penultimate and the second lattice sites have the unity distribution with $t = 0.05T$ and $0.95T$, respectively. Those results indicate that the gap state becomes an alternative state transfer channel between the photon states of $|0,0,0,\ldots,1,0\rangle_{31} \longrightarrow |0,1,0,\ldots,0,0\rangle_{31}$.

Actually, the numerical results can be understood physically as the following effective Hamiltonian of the photon-photon transfer (see Appendix D for details)

$$H_{\text{eff}}^{pp} = \sum_{n=2}^{N-1} J_1 a_n^{\dagger} b_n + \sum_{n=1}^{N-2} J_2 a_{n+1}^{\dagger} b_n + \text{H.c.}, \tag{29}$$

which excludes the first and last lattice sites to form the standard SSH model of the magnon-QED-circuit chain. More specifically by solving the Liouville equation, as shown in Fig. 14(d), the numerical result of distribution versus time confirms the achievement of photon-photon transfer via an alternative topologically protected channel. In contrast with the magnon-magnon transfer, defect-induced photon-photon transfer is on account of the virtual excitation of magnon.

From above numerical results and analysis, it seems that the magnon-photon and photon-magnon and the photon-photon transfers are different kinds of transfer processes, which are all satisfied with the large specific on-site potential defects in the defect SSH model. It is also significant to examine the effect of the defect strength imposed on the specific lattice site when the system is driven by the three-step protocol. As shown in Figs. 15(a)–15(c), we adopt J_0 to be the unit for parameters and observe that there are some regions of the defect strength w/J_0 and the total transfer time $J_0 t$ satisfying the high fidelity of

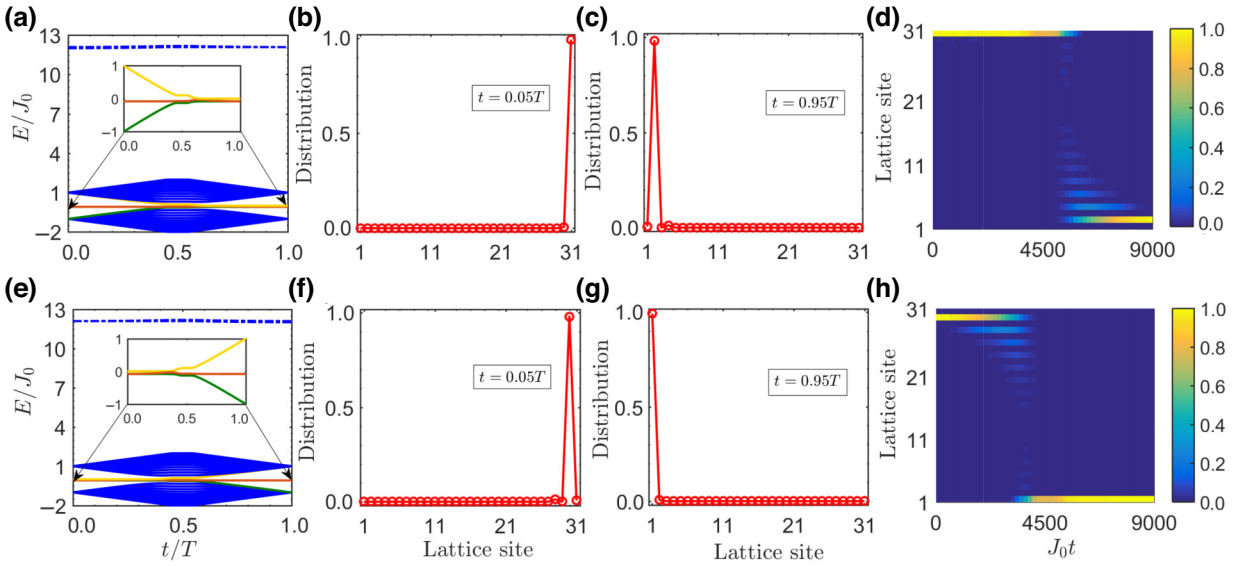

FIG. 13. The energy spectrum as a function of time when the chain possesses defects on the lattice site A_1 and B_{30} for magnon-photon transfer in (a) and the lattice site B_1 and A_{31} for photon-magnon transfer in (e). The distributions of the gap state at $t = 0.05T, 0.95T$ for magnon-photon transfer in (b),(c) and for photon-magnon transfer in (f),(g), respectively. The magnon-photon transfer process between $|0,0,0,\ldots,0,1\rangle_{31}$ and $|0,1,0,\ldots,0,0\rangle_{31}$ and the photon-magnon transfer process between $|0,0,0,\ldots,1,0\rangle_{31}$ and $|1,0,0,\ldots,0,0\rangle_{31}$ as a function of time in (d),(h), respectively. We chose the defect strength $w = 12J_0$ and the chain with the size of $L = 2N - 1 = 31$ is employed by the three-step protocol.

the magnon-photon, the photon-magnon and the photon-photon transfer, respectively. Learning from the effective Hamiltonian of defect-induced magnon-photon and photon-magnon transfer in Eq. (28), it is expected that the varying parameters versus the transfer fidelity shows exactly the same numerical results in response to these two kinds of transfer processes in Figs. 15(a) and 15(b). As for the defect-induced photon-photon transfer, the varying parameters versus the transfer fidelity appears with some different numerical results comparing with the two former transfer processes. In the scope of Figs. 15(a) and 15(b) for investigating the magnon-photon and photon-magnon transfers, the value of defect strength within an appropriate range cannot only effectively improve the fidelity but also shorten the transfer time. However, by gradually pursuing higher-fidelity transfer, the larger value of defect strength and the longer transfer time are demanded. Specially, we plot the 0.995 and 0.997 fidelity contour lines of the magnon-photon and photon-magnon transfer in Figs. 15(a) and 15(b), respectively. Transfer fidelities with $F_{mp(pm)} \geqslant 0.995$ emerge by the around ranges of $w/J_0 \in [20, 30] \cap J_0t[5500, 10000]$. With regard to the photon-photon transfer process, the larger value of defect strength and the longer transfer time are still required for high-fidelity transfer. Analogously, by examination with the 0.995 and 0.997 fidelity contour lines in Fig. 15(c), the oscillation on the fidelity of photon-photon transfer is bound up with the transfer time. The reason lies in the fact that the fast

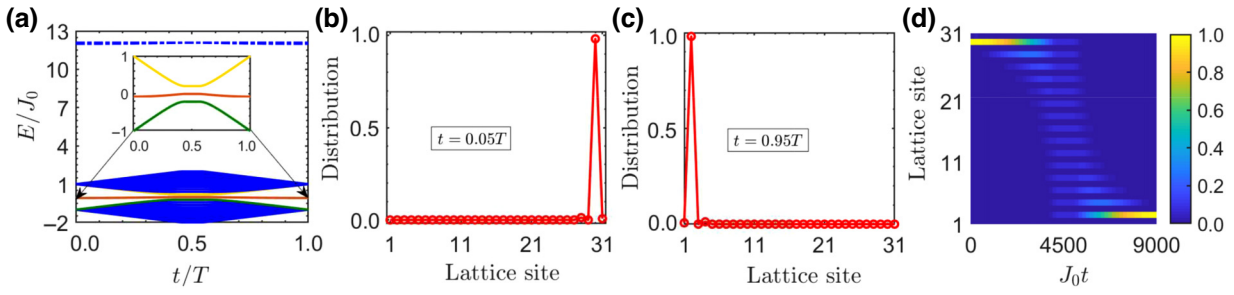

FIG. 14. (a) The energy spectrum as a function of time for the three-step protocol when the chain possesses defects on the lattice site B_1 and A_{31}. (b),(c) The distributions of the gap state for different time with $t = 0.05T$ and $t = 0.95T$, respectively. (d) The photon-photon transfer process between $|0,0,0,\ldots,1,0\rangle_{31}$ and $|0,1,0,\ldots,0,0\rangle_{31}$ as a function of time. We chose the defect strength $w = 12J_0$ and the chain with the size of $L = 2N - 1 = 31$ is employed by the three-step protocol.

oscillating terms are safely negligible due to the long transfer time in Eq. (D2), otherwise those terms may destroy the fidelity greatly with $J_0 t \leqslant 6500$ in Fig. 15(c). At the same time, it is no wonder that the 0.997 fidelity contour line shows more evident oscillation than the 0.995 fidelity contour line. Clearly, the above numerical results are consistent with the analysis of effective Hamiltonian of whether the magnon-photon and photon-magnon transfer or the photon-photon transfer, except for some regions where the photon-photon transfer is not exactly equivalent to the former two defect-induced transfers owing to the different intrinsic physics of transfer processes. Nevertheless, the improvement of defect-induced transfer speed based on the other protocols has no outstanding numerical results due to the fact that the above fast topological QSTs take account of the standard rather than defect SSH model. This reveals that our approach provides a flexible tunability of different defect-induced transfers in the magnon-QED-circuit chain, and thus could enable a number of applications in the quantum control of hybrid system as well as the topological matter.

VI. CONCLUSION

To summarize, we have proposed a magnon-circuit-QED chain arranging two YIG spheres at both ends of the chain and superconducting resonators at the middle in one-dimensional space, which can be quantized into a standard SSH model with time-dependent couplings. We analytically derive that the hybrid system can be expressed as a two-band structure in momentum space, and its trivial and nontrivial topological phases can be characterized by the Zak phases equal to 0 and π, respectively. According to the energy-spectrum characteristics of the system, the time-dependent magnon-photon and photon-photon couplings, which can be realized by the Kerr nonlinearity characteristic of YIG spheres and SQUIDs, are properly designed so that fast topological magnon-magnon QST can be realized by the edge channel. The numerical results show that the fidelity, robustness, and speed of the magnon-magnon transfer can be improved to different degrees by different coupling protocols in case of not only single excitation. In particular, the multiexcitation magnon-magnon transfer can also be realized in the fast and topologically protected way employing by three-step protocol. Furthermore, when larger on-site defects are added to different types of lattice sites in the two ends, alternative single-excitation QSTs in respect to magnon-photon, photon-magnon, and photon-photon transfers can be generated by the topologically protected edge channel. Our work, introducing fast topological pumping into constructing different types of excitation transfer in magnon-circuit-QED hybrid system with topological states of matter, paves a promising way to realize fast, robust, and controllable quantum information processing in magnetics and optics.

ACKNOWLEDGMENTS

This work was supported by National Natural Science Foundation of China (NSFC) (Grants No. 11675046 and No. 12304407), Program for Innovation Research of Science in Harbin Institute of Technology (Grant No. A201412), Postdoctoral Scientific Research Developmental Fund of Heilongjiang Province (Grant No. LBH-Q15060), and the China Postdoctoral Science Foundation (Grant No. 2023TQ0310).

APPENDIX A: VERIFICATION OF COMPATIBILITY BETWEEN SQUEEZED FRAME AND LABORATORY FRAME

In order to prove that the squeezed frame of the first and end lattice sites are compatible with the laboratory frame of the bulk, we take the two-body Hamiltonian as an example. Then, the Hamiltonian of one magnon mode and one photon mode can be written as in the laboratory

$$H^{\text{lab}} = \Delta_a a^\dagger a + \omega_b b^\dagger b + J_1(ab^\dagger + a^\dagger b) + \tilde{K}(a^\dagger a^\dagger + aa)/2 - ir_p^{\cdot}(a^{\dagger 2} - a^2)/2, \quad \text{(A1)}$$

where $\tilde{\Delta}_a$ is the detuning between the drive field and the magnon mode. Then, the Hamiltonian of one magnon mode and one photon mode can be diagonalized in the squeeze framework by introducing the Bogoliubov squeezing transformation $a = a_s \cosh(r_p) + a_s^\dagger \sinh(r_p)$ as

$$H^{\text{squ}} = \tilde{\Delta}_s a^\dagger a + \omega_b b^\dagger b + J_0 b^\dagger(\cosh(r_p)a^\dagger - \sinh(r_p)a) + J_0 b(\cosh(r_p)a - \sinh(r_p)a^\dagger) + \tilde{K}(a^\dagger a^\dagger + aa)/2, \quad \text{(A2)}$$

where $\Delta_s = \sqrt{\tilde{\Delta}_a^2 - \tilde{K}^2}$. In Fig. 16, we assume the total evolution time $T = 20/J_0$ and other parameters are chosen as $\Delta_a = \tilde{\Delta}_s = \omega_b/2\pi = 30J_0$ for convenience to satisfy the rotating-wave approximation. Furthermore, the squeezed parameter r and the Kerr coefficient satisfies the following functional relation: $r_p(t) = \text{arc}\sinh[J_1(t)]$. We compare the time evolution of populations for $|01\rangle_{a_s,b}$ and $|10\rangle_{a_s,b}$ with the Hamiltonian H^{squ} in the squeezed frame, and for $|01\rangle_{a,b}$ and $|10\rangle_{a,b}$ with the Hamiltonian H^{lab} in the laboratory frame shown in Figs. 16(a) and 16(b), respectively. As expected, one can see that solid and dotted lines coincide exactly in the squeezed and laboratory frames, which proves the compatibility of those frames.

APPENDIX B: DERIVATION OF ZERO-MODE EDGE STATE

For the odd-sized magnon-QED-circuit chain, the translational invariance of the system suggests the following

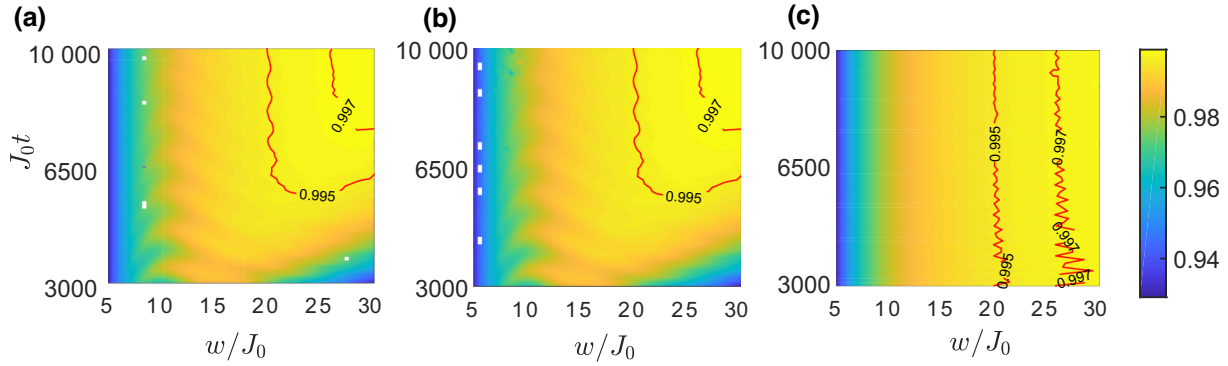

FIG. 15. The fidelity versus the varying defect strength w/J_0 and the transfer time J_0t for (a) the magnon-photon transfer, (b) the photon-magnon transfer and (c) the photon-photon transfer. The chain with the size of $L = 2N - 1 = 31$ is employed by the three-step protocol.

ansatz for an eigenstate of edge state:

$$|\varphi_E\rangle = \sum_{n=1}^{N} \lambda^n (\alpha a_n^\dagger + \beta b_n^\dagger)|G\rangle, \tag{B1}$$

where $|G\rangle = |0, 0, 0 \cdots\rangle$ denotes a decoupled state of the magnon-QED-circuit chain with all lattice sites in zero-photon (magnon) Fock state for the even (odd) lattice site and λ denotes the localization indexes. The probability amplitude on the site n decays (increases) exponentially with the distance n when $\lambda < 1$ ($\lambda > 1$), with respect to the left (right) edge state, when the wave function is normalized. Through the eigenvalue equation $E|\varphi_E\rangle = H_I|\varphi_E\rangle$, one can obtain

$$\begin{aligned} &E\lambda^n(\alpha a_n^\dagger + \beta b_n^\dagger)|G\rangle \\ &= \left[J_1\lambda^n(\beta a_n^\dagger + \alpha b_n^\dagger) + J_2(\beta\lambda^{n-1}a_n^\dagger + \alpha\lambda^{n+1}b_n^\dagger)\right]. \end{aligned} \tag{B2}$$

When $\alpha = 0$ ($\beta = 0$), according to Eq. (B1) the YIG sphere (superconducting resonator) are occupied by the edge state whose eigenenergy is $E = 0$. For the odd-sized chain, both the left and right edge states occupy the YIG spheres in each unit cell, resulting to $\alpha = 1$ and $\beta = 0$ in Eq. (B1). With this analysis, we can obtain $J_1 + J_2\lambda = 0$. Thus, the edge-state wave function by occupying the YIG sphere then can be derived as

$$|\varphi_E\rangle = \sum_{n=1}^{N} (-\lambda)^n a_n^\dagger |G\rangle, \tag{B3}$$

where $\lambda = J_1/J_2$.

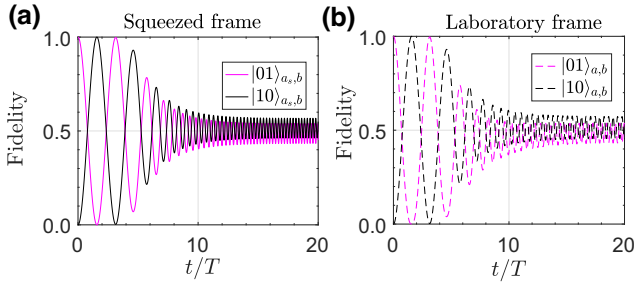

FIG. 16. Time evolution of populations for $|01\rangle_{a_s,b}$ and $|10\rangle_{a_s,b}$ with the Hamiltonian H^{squ} of the squeezed frame in (a) and for $|01\rangle_{a_s,b}$ and $|10\rangle_{a_s,b}$ with the Hamiltonian H^{squ} of the laboratory frame in (b). We choose the total evolution time $T = 10/J_0$, and other parameters are chosen as $\Delta_a = \tilde{\Delta}_s = \omega_b/2\pi = 30J_0$ for convenience to satisfy the rotating-wave approximation.

APPENDIX C: EFFECTIVE HAMILTONIAN DERIVATION OF MAGNON-PHOTON AND PHOTON-MAGNON TRANSFERS

In order to realize magnon-photon (photon-magnon) transfer in the magnon-QED-circuit chain, the on-site potential defects are added on the first lattice cell for YIG sphere A_1 and the penultimate lattice cell for superconducting resonator B_{N-1} (the first lattice cell for superconducting resonator B_2 and the last lattice cell for YIG sphere A_N), whose the full Hamiltonian can be written as

$$\begin{aligned} H_{\text{full}} = &\sum_{i,j}(w_{a,i}a_i^\dagger a_i + w_{b,j}b_j^\dagger b_j) + \sum_{n=1}^{N-1}\left(J_1 a_n^\dagger b_n\right. \\ &\left. + J_2 a_{n+1}^\dagger b_n\right) + \text{H.c.}, \end{aligned} \tag{C1}$$

where $i = 1$ and $j = N - 1$ ($i = N$ and $j = 1$) indicates the conditions of defect lattice cell for realizing the magnon-photon (photon-magnon) transfer, respectively. By performing a unitary transformation $U_1 =$

$\exp\{-it[\sum_{i,j}(w_{a,i}a_i^\dagger a_i + w_{b,j}b_j^\dagger b_j)]\}$, the system Hamiltonian for the photon-magnon and the magnon-photon transfers can be further represented as, respectively,

$$H^{mp} = J_1 a_1^\dagger b_1 e^{iw_{a,1}t} + J_1 a_{N-1}^\dagger b_{N-1} e^{-iw_{b,N-1}t} + J_2 a_N^\dagger b_{N-1} e^{-iw_{b,N-1}t} + \sum_{n=2}^{N-2} J_1 a_n^\dagger b_n + \sum_{n=1}^{N-2} J_2 a_{n+1}^\dagger b_n + \text{H.c.}, \tag{C2}$$

$$H^{pm} = J_1 a_1^\dagger b_1 e^{-iw_{b,1}t} + J_2 a_2^\dagger b_1 e^{-iw_{b,1}t} + J_2 a_N^\dagger b_{N-1} e^{iw_{a,N}t} + \sum_{n=2}^{N-1} J_1 a_n^\dagger b_n + \sum_{n=2}^{N-2} J_2 a_{n+1}^\dagger b_n + \text{H.c.}. \tag{C3}$$

In order to realize the photon-magnon and magnon-photon transfer, the value of detunings needs to be as large as possible to satisfy the condition $|w_{a(b),i(j)}| \gg J_{1,2}$. According to the theory of second-order perturbation [101], the Hamiltonian can be reduced into, respectively,

$$H_{\text{eff}}^{mp} = J_{\text{eff}}^{mp} a_{N-1}^\dagger a_N + \sum_{n=2}^{N-2} J_1 a_n^\dagger b_n + \sum_{n=1}^{N-2} J_2 a_{n+1}^\dagger b_n + \text{H.c.}, \tag{C4}$$

$$H_{\text{eff}}^{pm} = J_{\text{eff}}^{pm} a_1^\dagger a_3 + \sum_{n=2}^{N-1} J_1 a_n^\dagger b_n + \sum_{n=2}^{N-2} J_2 a_{n+1}^\dagger b_n + \text{H.c.}, \tag{C5}$$

where $J_{\text{eff}}^{mp(pm)} = J_1 J_2 / w_{b,N-1(1)}$.

APPENDIX D: EFFECTIVE HAMILTONIAN DERIVATION OF PHOTON-PHOTON TRANSFER

As for the photon-photon transfer in the magnon-QED-circuit chain, the on-site potential defects are added on the first lattice site A_1 and the last lattice site A_N. The full Hamiltonian can be written as

$$H_{\text{Full}}^{pp} = \sum_i w_{a,i} a_i^\dagger a_i + \sum_{n=1}^{N-1} (J_1 a_n^\dagger b_n + J_2 a_{n+1}^\dagger b_n) + \text{H.c.}, \tag{D1}$$

where $i = 1, N$ indicates the condition of defect lattice cell for realizing the photon-photon transfer. Then, we perform a unitary transformation $U_2 = \exp[-it(\sum_i w_{a,i} a_i^\dagger a_i)]$, the system Hamiltonian reads

$$H^{pp} = J_1 a_1^\dagger b_1 e^{iw_{a,i}t} + J_2 a_N^\dagger b_{N-1} e^{iw_{a,N}t} + \sum_{n=2}^{N-1} J_1 a_n^\dagger b_n + \sum_{n=1}^{N-2} J_2 a_{n+1}^\dagger b_n + \text{H.c.}. \tag{D2}$$

Considering the large detuning condition $|w_{a,i}| \gg J_{1,2}$, we can neglect the fast oscillating terms so that the effective Hamiltonian of photon-photon transfer can be safely obtained by

$$H_{\text{eff}}^{pp} = \sum_{n=2}^{N-1} J_1 a_n^\dagger b_n + \sum_{n=1}^{N-2} J_2 a_{n+1}^\dagger b_n + \text{H.c.} \tag{D3}$$

[1] Petr Král, Ioannis Thanopulos, and Moshe Shapiro, Colloquium: Coherently controlled adiabatic passage, Rev. Mod. Phys. **79**, 53 (2007).

[2] Hui Dong, Da-Zhi Xu, Jin-Feng Huang, and Chang-Pu Sun, Coherent excitation transfer via the dark-state channel in a bionic system, Light Sci. Appl. **1**, e2 (2012).

[3] Sougato Bose, Quantum communication through an unmodulated spin chain, Phys. Rev. Lett. **91**, 207901 (2003).

[4] Matthias Christandl, Nilanjana Datta, Artur Ekert, and Andrew J. Landahl, Perfect state transfer in quantum spin networks, Phys. Rev. Lett. **92**, 187902 (2004).

[5] Sougato Bose, Quantum communication through spin chain dynamics: an introductory overview, Contemp. Phys. **48**, 13 (2007).

[6] N. Y. Yao, L. Jiang, A. V. Gorshkov, Z.-X. Gong, A. Zhai, L.-M. Duan, and M. D. Lukin, Robust quantum state transfer in random unpolarized spin chains, Phys. Rev. Lett. **106**, 040505 (2011).

[7] S. Lorenzo, T. J. G. Apollaro, A. Sindona, and F. Plastina, Quantum-state transfer via resonant tunneling through local-field-induced barriers, Phys. Rev. A **87**, 042313 (2013).

[8] M. P. Silveri, K. S. Kumar, J Tuorila, J. Li, A. Vepsäläinen, E. V. Thuneberg, and G. S. Paraoanu, Stückelberg interference in a superconducting qubit under periodic latching modulation, New J. Phys. **17**, 043058 (2015).

[9] Jin-Xuan Han, Jin-Lei Wu, Yan Wang, Yan Xia, Yong-Yuan Jiang, and Jie Song, Large-scale Greenberger-Horne-Zeilinger states through a topologically protected zero-energy mode in a superconducting qutrit-resonator chain, Phys. Rev. A **103**, 032402 (2021).

[10] J. I. Cirac, P. Zoller, H. J. Kimble, and H. Mabuchi, Quantum state transfer and entanglement distribution among distant nodes in a quantum network, Phys. Rev. Lett. **78**, 3221 (1997).

[11] D. N. Matsukevich and A. Kuzmich, Quantum state transfer between matter and light, Science **306**, 663 (2004).

[12] Lin Tian, Optoelectromechanical transducer: Reversible conversion between microwave and optical photons, Ann. Phys.(Berlin, Ger.) **527**, 1 (2015).

[13] B. Vermersch, P.-O. Guimond, H. Pichler, and P. Zoller, Quantum state transfer via noisy photonic and phononic waveguides, Phys. Rev. Lett. **118**, 133601 (2017).

[14] Ze-Liang Xiang, Mengzhen Zhang, Liang Jiang, and Peter Rabl, Intracity quantum communication via thermal microwave networks, Phys. Rev. X **7**, 011035 (2017).

[15] Bing Chen, Wei Fan, Yan Xu, Zhao-yang Chen, Xun-li Feng, and C. H. Oh, Long-range adiabatic quantum state transfer through a tight-binding chain as a quantum data bus, Phys. Rev. A **86**, 012302 (2012).

[16] K Eckert, O Romero-Isart, and A Sanpera, Efficient quantum state transfer in spin chains via adiabatic passage, New J. Phys. **9**, 155 (2007).

[17] G. Della Valle, M. Ornigotti, T. Toney Fernandez, P. Laporta, S. Longhi, A. Coppa, and V. Foglietti, Adiabatic light transfer via dressed states in optical waveguide arrays, Appl. Phys. Lett. **92**, 011106 (2008).

[18] Guilherme M. A. Almeida, Francesco Ciccarello, Tony J. G. Apollaro, and Andre M. C. Souza, Quantum-state transfer in staggered coupled-cavity arrays, Phys. Rev. A **93**, 032310 (2016).

[19] Jin-Lei Wu, Xin Ji, and Shou Zhang, Fast adiabatic quantum state transfer and entanglement generation between two atoms via dressed states, Sci. Rep. **7**, 46255 (2017).

[20] R. R. Agundez, C. D. Hill, L. C. L. Hollenberg, S. Rogge, and M. Blaauboer, Superadiabatic quantum state transfer in spin chains, Phys. Rev. A **95**, 012317 (2017).

[21] M. H. Devoret and R. J. Schoelkopf, Superconducting circuits for quantum information: An outlook, Science **339**, 1169 (2013).

[22] S. Stobbe, P. Lodahl, S. Mahmoodian, A. Rauschenbeutel, P. Schneeweiss, J. Volz, H. Pichler, and P. Zoller, Chiral quantum optics, Nature **541**, 473 (2017).

[23] J. Gorman, D. G. Hasko, and D. A. Williams, Charge-qubit operation of an isolated double quantum dot, Phys. Rev. Lett. **95**, 090502 (2005).

[24] Zhongyuan Zhou, Shih-I Chu, and Siyuan Han, Quantum computing with superconducting devices: A three-level SQUID qubit, Phys. Rev. B **66**, 054527 (2002).

[25] M. A. Nielsen and I. L. Chuang, *Quantum Computation and Quantum Information* (Cambridge University Press, Cambridge, England, 2010).

[26] Yutaka Tabuchi, Seiichiro Ishino, Toyofumi Ishikawa, Rekishu Yamazaki, Koji Usami, and Yasunobu Nakamura, Hybridizing ferromagnetic magnons and microwave photons in the quantum limit, Phys. Rev. Lett. **113**, 083603 (2014).

[27] Yutaka Tabuchi, Seiichiro Ishino, Atsushi Noguchi, Toyofumi Ishikawa, Rekishu Yamazaki, Koji Usami, and Yasunobu Nakamura, Coherent coupling between a ferromagnetic magnon and a superconducting qubit, Science **349**, 405 (2015).

[28] Dany Lachance-Quirion, Yutaka Tabuchi, Seiichiro Ishino, Atsushi Noguchi, Toyofumi Ishikawa, Rekishu Yamazaki, and Yasunobu Nakamura, Resolving quanta of collective spin excitations in a millimeter-sized ferromagnet, Sci. Adv. **3**, e1603150 (2017).

[29] A. Wallraff, D. I. Schuster, A. Blais, L. Frunzio, R.-S. Huang, J. Majer, S. Kumar, S. M. Girvin, and R. J. Schoelkopf, Strong coupling of a single photon to a superconducting qubit using circuit quantum electrodynamics, Nature **431**, 162 (2004).

[30] Yi Li, Tomas Polakovic, Yong-Lei Wang, Jing Xu, Sergi Lendinez, Zhizhi Zhang, Junjia Ding, Trupti Khaire, Hilal Saglam, Ralu Divan, John Pearson, Wai-Kwong Kwok, Zhili Xiao, Valentine Novosad, Axel Hoffmann, and Wei Zhang, Strong coupling between magnons and microwave photons in on-chip ferromagnet-superconductor thin-film devices, Phys. Rev. Lett. **123**, 107701 (2019).

[31] Justin T. Hou and Luqiao Liu, Strong coupling between microwave photons and nanomagnet magnons, Phys. Rev. Lett. **123**, 107702 (2019).

[32] Y. Yang, J. W. Rao, Y. S. Gui, B. M. Yao, W. Lu, and C.-M. Hu, Control of the magnon-photon level attraction in a planar cavity, Phys. Rev. Appl. **11**, 054023 (2019).

[33] L. McKenzie-Sell, J. Xie, C.-M. Lee, J. W. A. Robinson, C. Ciccarelli, and J. A. Haigh, Low-impedance superconducting microwave resonators for strong coupling to small magnetic mode volumes, Phys. Rev. B **99**, 140414(R) (2019).

[34] Yi Li, Volodymyr G. Yefremenko, Marharyta Lisovenko, Cody Trevillian, Tomas Polakovic, Thomas W. Cecil, Peter S. Barry, John Pearson, Ralu Divan, Vasyl Tyberkevych, Clarence L. Chang, Ulrich Welp, Wai-Kwong Kwok, and Valentine Novosad, Coherent coupling of two remote magnonic resonators mediated by superconducting circuits, Phys. Rev. Lett. **128**, 047701 (2022).

[35] J. H. Wesenberg, A. Ardavan, G. A. D. Briggs, J. J. L. Morton, R. J. Schoelkopf, D. I. Schuster, and K. Mølmer, Quantum computing with an electron spin ensemble, Phys. Rev. Lett. **103**, 070502 (2009).

[36] Dany Lachance-Quirion, Samuel Piotr Wolski, Yutaka Tabuchi, Shingo Kono, Koji Usami, and Yasunobu Nakamura, Entanglement-based single-shot detection of a single magnon with a superconducting qubit, Science **367**, 425 (2020).

[37] Jin-Xuan Han, Jin-Lei Wu, Yan Wang, Yan Xia, Yong-Yuan Jiang, and Jie Song, Tripartite high-dimensional magnon-photon entanglement in phases with broken $\mathcal{PT}$-symmetry of a non-Hermitian hybrid system, Phys. Rev. B **105**, 064431 (2022).

[38] Atac Imamoğlu, Cavity QED based on collective magnetic dipole coupling: Spin ensembles as hybrid two-level systems, Phys. Rev. Lett. **102**, 083602 (2009).

[39] D. I. Schuster, A. P. Sears, E. Ginossar, L. DiCarlo, L. Frunzio, J. J. L. Morton, H. Wu, G. A. D. Briggs, B. B. Buckley, D. D. Awschalom, and R. J. Schoelkopf, High-cooperativity coupling of electron-spin ensembles to superconducting cavities, Phys. Rev. Lett. **105**, 140501 (2010).

[40] Y. Kubo, F. R. Ong, P. Bertet, D. Vion, V. Jacques, D. Zheng, A. Dréau, J.-F. Roch, A. Auffeves, F. Jelezko, J. Wrachtrup, M. F. Barthe, P. Bergonzo, and D. Esteve, Strong coupling of a spin ensemble to a superconducting resonator, Phys. Rev. Lett. **105**, 140502 (2010).

[41] S. Probst, H. Rotzinger, S. Wünsch, P. Jung, M. Jerger, M. Siegel, A. V. Ustinov, and P. A. Bushev, Anisotropic rare-earth spin ensemble strongly coupled to a superconducting resonator, Phys. Rev. Lett. **110**, 157001 (2013).

[42] R. M. White, *Quantum Theory of Magnetism: Magnetic Properties of Materials, 3rd Ed* (Springer, Berlin, 2007).

[43] Feng-Yang Zhang, Ye-Xiong Zeng, and Qi-Cheng Wu, Chui-Ping Yang, Cat-state encoding of a quantum information processor module with cavity–magnon system, Appl. Phys. Lett. **122**, 084001 (2023).

[44] A. G. Gurevich and G. A. Melkov, *Magnetization Oscillations and Waves* (CRC, Florida, 1996).

[45] Hans Huebl, Christoph W. Zollitsch, Johannes Lotze, Fredrik Hocke, Moritz Greifenstein, Achim Marx, Rudolf Gross, and Sebastian T. B. Goennenwein, High cooperativity in coupled microwave resonator ferrimagnetic insulator hybrids, Phys. Rev. Lett. **111**, 127003 (2013).

[46] Xufeng Zhang, Chang-Ling Zou, Liang Jiang, and Hong X. Tang, Strongly coupled magnons and cavity microwave photons, Phys. Rev. Lett. **113**, 156401 (2014).

[47] Philipp Pirro, Vitaliy I. Vasyuchka, Alexander A. Serga, and Burkard Hillebrands, Advances in coherent magnonics, Nat. Rev. Mater. **6**, 2058 (2021).

[48] Dany Lachance-Quirion, Yutaka Tabuchi, Arnaud Gloppe, Koji Usami, and Yasunobu Nakamura, Hybrid quantum systems based on magnonics, Appl. Phys. Express **12**, 070101 (2019).

[49] Yutaka Tabuchi, Seiichiro Ishino, Atsushi Noguchi, Toyofumi Ishikawa, Rekishu Yamazaki, Koji Usami, and Yasunobu Nakamura, Coherent coupling between a ferromagnetic magnon and a superconducting qubit, Science **349**, 405 (2015).

[50] Yutaka Tabuchi, Seiichiro Ishino, Atsushi Noguchi, Toyofumi Ishikawa, Rekishu Yamazaki, Koji Usami, and Yasunobu Nakamura, Quantum magnonics: The magnon meets the superconducting qubit, C.R. Phys. **17**, 729 (2016).

[51] Xufeng Zhang, Chang-Ling Zou, Na Zhu, Florian Marquardt, Liang Jiang, and Hong X. Tang, Magnon dark modes and gradient memory, Nat. Commun. **6**, 405 (2015).

[52] Yaacov E. Kraus, Yoav Lahini, Zohar Ringel, Mor Verbin, and Oded Zilberberg, Topological states and adiabatic pumping in quasicrystals, Phys. Rev. Lett. **109**, 106402 (2012).

[53] N. Y. Yao, C. R. Laumann, A. V. Gorshkov, H. Weimer, L. Jiang, J. I. Cirac, P. Zoller, and M. D. Lukin, Topologically protected quantum state transfer in a chiral spin liquid, Nat. Commun. **4**, 2041 (2013).

[54] Mor Verbin, Oded Zilberberg, Yoav Lahini, Yaacov E. Kraus, and Yaron Silberberg, Topological pumping over a photonic Fibonacci quasicrystal, Phys. Rev. B **91**, 064201 (2015).

[55] M. Bello, C. E. Creffield, and G. Platero, Long-range doublon transfer in a dimer chain induced by topology and ac fields, Sci. Rep. **6**, 22562 (2016).

[56] C. Dlaska, B. Vermersch, and P. Zoller, Robust quantum state transfer via topologically protected edge channels in dipolar arrays, Quantum Sci. Technol. **2**, 015001 (2017).

[57] Nicolai Lang and Hans Peter Büchler, Topological networks for quantum communication between distant qubits, Npj Quantum Inf. **3**, 2056 (2017).

[58] Marta P. Estarellas, Irene D'Amico, and Timothy P. Spiller, Topologically protected localised states in spin chains, Sci. Rep. **7**, 42904 (2017).

[59] Feng Mei, Gang Chen, Lin Tian, Shi-Liang Zhu, and Suotang Jia, Topology-dependent quantum dynamics and entanglement-dependent topological pumping in superconducting qubit chains, Phys. Rev. A **98**, 032323 (2018).

[60] Stefano Longhi, Gian Luca Giorgi, and Roberta Zambrini, Landau–Zener topological quantum state transfer, Adv. Quantum. Technol. **2**, 1800090 (2019).

[61] W. P. Su, J. R. Schrieffer, and A. J. Heeger, Solitons in polyacetylene, Phys. Rev. Lett. **42**, 1698 (1979).

[62] David Guery-Odelin, Stefano Longhi, Felippo M. D'Angelis, Felipe A. Pinheiro, and Francois Impens, Fast and robust quantum state transfer in a topological Su-Schrieffer-Heeger chain with next-to-nearest-neighbor interactions, Phys. Rev. Res. **2**, 033475 (2020).

[63] Stefano Longhi, Topological pumping of edge states via adiabatic passage, Phys. Rev. B **99**, 155150 (2019).

[64] Lijun Huang, Zhi Tan, Honghua Zhong, and Bo Zhu, Fast and robust quantum state transfer assisted by zero-energy interface states in a splicing Su-Schrieffer-Heeger chain, Phys. Rev. A **106**, 022419 (2022).

[65] N. E. Palaiodimopoulos, I. Brouzos, F. K. Diakonos, and G. Theocharis, Fast and robust quantum state transfer via a topological chain, Phys. Rev. A **103**, 052409 (2021).

[66] Guo-Qiang Zhang, Yi-Pu Wang, and J. Q. You, Theory of the magnon Kerr effect in cavity magnonics, Sci. China Phys. Mech. Astron. **62**, 987511 (2019).

[67] David D. Awschalom *et al.*, Quantum engineering with hybrid magnonic systems and materials (invited paper), IEEE Trans. Quantum Eng. **2**, 1 (2021).

[68] Yi-Pu Wang, Guo-Qiang Zhang, Dengke Zhang, Xiao-Qing Luo, Wei Xiong, Shuai-Peng Wang, Tie-Fu Li, C.-M. Hu, and J. Q. You, Magnon Kerr effect in a strongly coupled cavity-magnon system, Phys. Rev. B **94**, 224410 (2016).

[69] Charles Kittel, On the theory of ferromagnetic resonance absorption, Phys. Rev. **73**, 155 (1948).

[70] Ö. O. Soykal and M. E. Flatté, Strong field interactions between a nanomagnet and a photonic cavity, Phys. Rev. Lett. **104**, 077202 (2010).

[71] Ö. O. Soykal and M. E. Flatté, Size dependence of strong coupling between nanomagnets and photonic cavities, Phys. Rev. B **82**, 104413 (2010).

[72] Xiu Gu, Anton Frisk Kockum, Adam Miranowicz, Yu xi Liu, and Franco Nori, Microwave photonics with superconducting quantum circuits, Phys. Rep. **718-719**, 1 (2017).

[73] T. Holstein and H. Primakoff, Field dependence of the intrinsic domain magnetization of a ferromagnet, Phys. Rev. **58**, 1098 (1940).

[74] Jie Li, Shi-Yao Zhu, and G. S. Agarwal, Magnon-photon-phonon entanglement in cavity magnomechanics, Phys. Rev. Lett. **121**, 203601 (2018).

[75] Markus Aspelmeyer, Tobias J. Kippenberg, and Florian Marquardt, Cavity optomechanics, Rev. Mod. Phys. **86**, 1391 (2014).

[76] M. O. Scully and M. S. Zubairy, *Quantum Optics* (Cambridge University, Cambridge, England, 1997).

[77] Borja Peropadre, David Zueco, Friedrich Wulschner, Frank Deppe, Achim Marx, Rudolf Gross, and Juan José García-Ripoll, Tunable coupling engineering between superconducting resonators: From sidebands to effective gauge fields, Phys. Rev. B **87**, 134504 (2013).

[78] L Tian, M. S. Allman, and R. W. Simmonds, Parametric coupling between macroscopic quantum resonators, New J. Phys. **10**, 115001 (2008).

[79] Alec Maassen van den Brink, A. J. Berkley, and M Yalowsky, Mediated tunable coupling of flux qubits, New J. Phys. **7**, 230 (2005).

[80] Matthias Schwarz, Manuel J. Pernpeintner, Edwar Xie, Ling Zhong, Christoph W. Zollitsch, Borja Peropadre, Juan-Jose Garcia Ripoll, Enrique Solano, Kirill G. Fedorov, Frank Menzel, Edwin P. Deppe, Achim Marx, and Rudolf Gross, Tunable coupling of transmission-line microwave resonators mediated by an rf SQUID, EPJ Quantum Technol. **3**, 8 (2016).

[81] L. DiCarlo, J. M. Chow, J. M. Gambetta, Lev S. Bishop, B. R. Johnson, D. I. Schuster, J. Majer, A. Blais, L. Frunzio, S. M. Girvin, and R. J. Schoelkopf, Demonstration of two-qubit algorithms with a superconducting quantum processor, Nature **460**, 240 (2009).

[82] Alexander Altland and Martin R. Zirnbauer, Nonstandard symmetry classes in mesoscopic normal-superconducting hybrid structures, Phys. Rev. B **55**, 1142 (1997).

[83] Shinsei Ryu and Yasuhiro Hatsugai, Topological origin of zero-energy edge states in particle-hole symmetric systems, Phys. Rev. Lett. **89**, 077002 (2002).

[84] J. Zak, Berry's phase for energy bands in solids, Phys. Rev. Lett. **62**, 2747 (1989).

[85] Di Xiao, Ming-Che Chang, and Qian Niu, Berry phase effects on electronic properties, Rev. Mod. Phys. **82**, 1959 (2010).

[86] P. Delplace, D. Ullmo, and G. Montambaux, Zak phase and the existence of edge states in graphene, Phys. Rev. B **84**, 195452 (2011).

[87] S. Q. Shen, *Topological Insulators: Dirac Equation in Condensed Matters* (Springer-Verlag Berlin Heidelberg, Berlin, 2012).

[88] T. L. Hughes, *Topological Insulators and Topological Superconductors* (Princeton University Press, Princeton, 2013).

[89] János K. Asbóth, László Oroszlány, and András Pályi, A short course on topological insulators, Lect. Notes Phys. **919**, 85 (2016).

[90] Feng Mei, Gang Chen, Lin Tian, Shi-Liang Zhu, and Suo tang Jia, Robust quantum state transfer via topological edge states in superconducting qubit chains, Phys. Rev. A **98**, 012331 (2018).

[91] P. J. Leek, M. Baur, J. M. Fink, R. Bianchetti, L. Steffen, S. Filipp, and A. Wallraff, Cavity quantum electrodynamics with separate photon storage and qubit readout modes, Phys. Rev. Lett. **104**, 100504 (2010).

[92] Rui-Chang Shen, Yi-Pu Wang, Jie Li, Shi-Yao Zhu, G. S. Agarwal, and J. Q. You, Long-time memory and ternary logic gate using a multistable cavity magnonic system, Phys. Rev. Lett. **127**, 183202 (2021).

[93] I. Brouzos, I. Kiorpelidis, F. K. Diakonos, and G. Theocharis, Fast, robust, and amplified transfer of topological edge modes on a time-varying mechanical chain, Phys. Rev. B **102**, 174312 (2020).

[94] D. L. Underwood, W. E. Shanks, Jens Koch, and A. A. Houck, Low-disorder microwave cavity lattices for quantum simulation with photons, Phys. Rev. A **86**, 023837 (2012).

[95] Sebastian Schmidt and Jens Koch, Circuit QED lattices: Towards quantum simulation with superconducting circuits, Ann. Phys.(Berlin) **525**, 395 (2013).

[96] Peng-Chao Xu, J. W. Rao, Y. S. Gui, Xiaofeng Jin, and C.-M. Hu, Cavity-mediated dissipative coupling of distant magnetic moments: Theory and experiment, Phys. Rev. B **100**, 094415 (2019).

[97] Jiannis Pachos and Herbert Walther, Quantum computation with trapped ions in an optical cavity, Phys. Rev. Lett. **89**, 187903 (2002).

[98] Xi-Rong Huang, Zong-Xing Ding, Chang-Sheng Hu, Li-Tuo Shen, Weibin Li, Huaizhi Wu, and Shi-Biao Zheng, Robust Rydberg gate via Landau-Zener control of Förster resonance, Phys. Rev. A **98**, 052324 (2018).

[99] Alexander P. M. Place *et al.*, New material platform for superconducting transmon qubits with coherence times exceeding 0.3 milliseconds, Nat. Commun. **12**, 1779 (2021).

[100] Helin Zhang, Srivatsan Chakram, Tanay Roy, Nathan Earnest, Yao Lu, Ziwen Huang, D. K. Weiss, Jens Koch, and David I. Schuster, Universal fast-flux control of a coherent, low-frequency qubit, Phys. Rev. X **11**, 011010 (2021).

[101] D. F. James and J Jerke, Effective hamiltonian theory and its applications in quantum information, Can. J. Phys. **85**, 625 (2007).